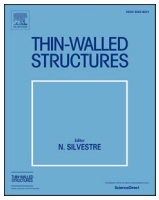
Thin–Walled Structures 209 (2025) 112907



Contents lists available at ScienceDirect

Thin-Walled Structures

journal homepage: www.elsevier.com/locate/tws



Full length article

High-cycle fatigue-constrained isogeometric topology optimization

Jinyu Gu [a,b], Jianghong Yang [a,b], Yingjun Wang [a,b,*]

[a] National Engineering Research Center of Novel Equipment for Polymer Processing, The Key Laboratory of Polymer Processing Engineering of the Ministry of Education, Guangdong Provincial Key Laboratory of Technique and Equipment for Macromolecular Advanced Manufacturing, South China University of Technology, Guangzhou, 510641, China

[b] School of Mechanical and Automotive Engineering, South China University of Technology, Guangzhou, 510641, China

ARTICLE INFO

Keywords:
High-cycle fatigue
Isogeometric topology optimization
Isogeometric analysis
Soderberg fatigue criterion
P-norm function

ABSTRACT

This paper focuses on the study of structural high-cycle fatigue problems commonly encountered in engineering and presents a fatigue-constrained isogeometric topology optimization (FCITO) method. First, the isogeometric analysis (IGA) framework for high-cycle fatigue problems is outlined. On this basis, a mathematical model for the FCITO method is established using the solid isotropic material with penalization (SIMP) method. The model aims to minimize compliance while considering volume and the Soderberg fatigue criterion constraints. Additionally, a modified P-norm function is employed to manage the numerous fatigue constraints, while the relaxation method is applied to address singularity issues. Moreover, the complete sensitivity equations for the objective function, volume constraint function, and fatigue constraint function are also provided. Finally, the effectiveness and capability of the presented FCITO method are demonstrated through several 2D and 3D examples.

1. Introduction

Topology optimization (TO) is an effective structural conceptual design approach that aims to find the optimal material distribution within a specified design domain to meet performance requirements [1,2]. Modern TO method originated from the seminal work by Bendsøe and Kikuchi in 1988 [3]. Over the past three decades, numerous new TO methods have emerged, including the solid isotropic material with penalization (SIMP) method [4], the evolutionary structural optimization (ESO) method [5], the level-set method (LSM) [6], and the moving morphable components/voids (MMC/V) methods [7,8]. TO methods have been applied to a wide range of physical problems, such as stiffness [9], vibration [10,11], stress [12–14], thermal conduction [15], fluid dynamics [16], and acoustics [17]. Among these, structural stiffness optimization has been extensively studied. However, in engineering practice, stiffness-based topology optimization alone is often insufficient. Many mechanical structures are subject to prolonged service periods, leading to potential fatigue damage [18,19]. Therefore, incorporating fatigue resistance into topology optimization is essential.

Currently, fatigue-constrained topology optimization (FCTO) methods have been developed and applied to various engineering problems [20,21], such as the fatigue optimization of lightweight aerial mounts [22,23], helicopter tail rotor pitch arms [24], engine connecting rods [25], and jacket support structure of offshore wind turbine [26]. In 2008, Desmorat et al. [27] were the first to integrate fatigue considerations into TO by employing Lemaitre's damage law to maximize structural fatigue life. Following this, Sherif et al. [28] introduced a method that converts dynamic loads into equivalent static loads to incorporate fatigue analysis into TO, enhancing structural fatigue resistance. James et al. [29] employed a coupled nonlinear brittle damage model within the framework of FCTO to simulate damage accumulation. Collet et al. [30] applied a modified Goodman fatigue criterion to address structural optimization problems under local fatigue constraints. Nabaki et al. [31] investigated the application of the modified Goodman fatigue criterion in topology optimization using the bi-directional evolutionary structural optimization (BESO) method. They further compared the impact of the Gerber fatigue criterion and the ASME-elliptic fatigue criterion on the resulting optimization outcomes [32]. Jeong et al. [33–36] explored fatigue damage under both proportional and nonproportional loads, implementing corresponding solutions in topology optimization. Chen et al. [37] developed a topology optimization framework for addressing Crossland fatigue constraints under proportional loading, based on the augmented Lagrangian method and the constrained natural element method. And, they further advanced this framework by incorporating multiaxial high-cycle fatigue criteria into topology optimization using the constrained natural

* Corresponding author.
E-mail address: wangyj84@scut.edu.cn (Y. Wang).

https://doi.org/10.1016/j.tws.2025.112907
Received 24 September 2024; Received in revised form 31 December 2024; Accepted 31 December 2024
Available online 1 January 2025
0263-8231/© 2025 Elsevier Ltd. All rights are reserved, including those for text and data mining, AI training, and similar technologies.

element method [38]. Additionally, various fatigue criterions, including Murakami's formula [39] and Soderberg's fatigue criterion [40], have been integrated into topology optimization to address different engineering challenges. On the other hand, several researchers have developed various TO methods focusing on fatigue damage accumulation [35,41–43]. Holmberg et al. [44] proposed a TO method aimed at mass minimization under fatigue constraints by integrating high-cycle fatigue analysis with principal stress calculations, based on the Palmgren-Miner rule. James and Waisman [45] presented a damage-based structural optimization method under multiple load cases. This method utilizes a coupled nonlinear brittle damage model to simulate damage accumulation, achieving minimum structural mass under damage constraints. Oest et al. [46,47] explored high-cycle fatigue damage in TO using the aggregation function and the Palmgren-Miner rule. Zhang et al. [48] introduced a FCTO method tailored for non-proportional cyclic loading, also grounded in the Palmgren-Miner rule. Chen et al. [49,50] examined the differences between the P-norm aggregation method and the augmented Lagrange method in addressing fatigue constraints in TO. Tauzowski et al. [51] incorporated structural reliability into the FCTO framework. Gu et al. [52] developed a novel FCTO method based on nonlinear fatigue damage rules. Furthermore, FCTO methods focused on fatigue damage accumulation techniques have been applied to various challenges, including multi-material design [53], flexible mechanisms design [54], and polygonal mesh structures [55].

Although significant advancements have been made in the development of TO methods with fatigue constraints, these methods have predominantly been built upon traditional finite element analysis (FEA) techniques. FEA relies on the element discretization of the geometric model, leading to an analysis model that only approximates the original geometry. Additionally, these elements are merely C^0-continuous with one another, which diminishes the accuracy of the analysis. To address these limitations, Hughes et al. presented the isogeometric analysis (IGA) method in 2005 [56]. This approach directly employs the non-uniform rational b-splines (NURBS) basis functions from the geometric model as the shape functions for analysis, thereby unifying the geometric and analytical models. In particular, the h-refinement scheme in NURBS basis functions enables rapid refinement of discrete meshes without affecting the underlying geometric model. Furthermore, the NURBS basis functions facilitate higher-order continuity between elements, enhancing the overall accuracy of the analysis [57]. This contributes to the accuracy of the fatigue analysis.

In 2010, Seo et al. [58] introduced the IGA method into TO and proposed the isogeometric topology optimization (ITO) method. Dedè et al. [59] implemented the ITO method for compliance problems using the phase-field model. Wang et al. [60] proposed an accurate and efficient ITO method based on the level set method and further investigated the ITO method for periodic lattice materials [61]. Subsequently, they introduced a human-aided design (HAD) approach, replacing traditional computer-aided design (CAD) in the ITO framework [62]. Gao et al. [63] explored a density-based ITO method and later developed ITO approaches for 2D and 3D metamaterials [64]. Hou et al. [65] proposed an explicit ITO method based on the MMC method. Qiu et al. [66] combined the ESO method to propose an ITO method with smooth boundary continuity. To date, ITO methods have been applied to various problems, including compliant mechanisms [67,68], shell structures [69,70], crack propagation [71], and multi-materials [72,73]. Notably, in recent years, some scholars have begun to consider structural strength in the ITO framework [74–76]. Liu et al. [77] presented an ITO method considering global stress constraints, while Villalba et al. [78] developed a material distribution-based ITO method that accounts for minimum weight and local stress constraints. Zhuang et al. [79] established a structural stress ITO method based on Bézier elements.

However, no research has yet addressed the critical issue of fatigue damage within the context of ITO methods, despite the fact that high-cycle fatigue is a common failure mode in engineering structures. This form of failure typically occurs under conditions of low stress (far below the yield stress) but with a high number of cycles. Therefore, it is essential to achieve the minimum cost structure while ensuring fatigue resistance. In this work, we exploit the advantages of IGA to present a fatigue-constrained ITO (FCITO) method. Specifically, we focus on high-cycle fatigue problems under proportional cyclic loading and establish a mathematical model for FCITO that targets structural compliance while considering fatigue and volume constraints. Additionally, the modified P-norm function is employed to handle local fatigue constraints, and sensitivity equations for both the objective and constraint functions are derived. Finally, the Method of Moving Asymptotes (MMA) [80,81] is used to solve the optimization model, and several examples are presented to validate the effectiveness of the proposed method.

The remainder of the paper is organized as follows. Section 2 provides a brief overview of the fundamental theory of IGA. Section 3 explains the relevant theories of high-cycle fatigue under proportional cyclic loading. Section 4 describes in detail the implementation and mathematical model of the presented FCITO method, along with the material interpolation scheme of the SIMP method and the fatigue constraint function. Subsequently, in Section 5, the sensitivity equations for the fatigue constraint function of the FCITO method are fully presented. In Section 6, several 2D and 3D examples are utilized to validate the effectiveness of the presented FCITO method. Finally, in Section 7, we summarize the conclusions of this study.

2. NURBS-based isogeometric analysis

Initially, we briefly introduce the basic theory of NURBS in Section 2.1. Then, an isogeometric structural mechanics analysis method based on NURBS is described in Section 2.2.

2.1. NURBS theory

NURBS, one of the commonly adopted curved surface representations in computer-aided design and computer graphics, is constructed from B-splines. For a non-decreasing sequence of real numbers (called the node vector) $\Xi = \left\{\xi_1, \xi_2, ..., \xi_{n+p+1}\right\}$ (where p is the order of B-spline basis functions, ξ_i is i-th knot values with $i = 1,2,...,n+p+1$), the 1D B-spline basis function $B_{i,p}(\xi)$ can be defined by the Cox-de Boor recursion equations as follows [56,82]:

$$B_{i,p}(\xi) = \begin{cases} 1 \text{ if} \xi_i \le \xi < \xi_{i+1} \\ 0 \text{ otherwise} \end{cases} \quad \text{for } p = 0 \tag{1}$$

$$B_{i,p}(\xi) = \frac{\xi - \xi_i}{\xi_{i+p} - \xi_i} B_{i,p-1}(\xi) + \frac{\xi_{i+p+1} - \xi}{\xi_{i+p+1} - \xi_{i+1}} B_{i+1,p-1}(\xi) \text{ for } p > 0 \tag{2}$$

where $\left[\xi_1, \xi_{n+p+1}\right]$ is a patch, $[\xi_i, \xi_{i+1})$ is the i-th knot span.

By assigning a weight ω_i to each basis function $B_{i,p}(\xi)$ one obtains the p-order NURBS basis functions as [83]:

$$N_{i,p}(\xi) = \frac{B_{i,p}(\xi)\omega_i}{\sum_{j=1}^{n} B_{j,p}(\xi)\omega_j} \tag{3}$$

Similarly, the 2D NURBS basis functions are constructed as:

$$N_{i,p}^{j,q}(\xi,\eta) = \frac{B_{i,p}(\xi)B_{j,q}(\eta)\omega_{i,j}}{\sum_{k=1}^{n}\sum_{l=1}^{m} B_{k,p}(\xi)B_{l,q}(\eta)\omega_{k,l}} \tag{4}$$

where $B_{i,p}(\xi)$ and $B_{j,q}(\eta)$ are B-spline basis functions defined in two directions (ξ and η), $\omega_{i,j}$ is the weight value corresponding to the tensor product $B_{i,p}(\xi)B_{j,q}(\eta)$.

Therefore, a NURBS surface of order p in the ξ direction and order q in the η direction is expressed as:

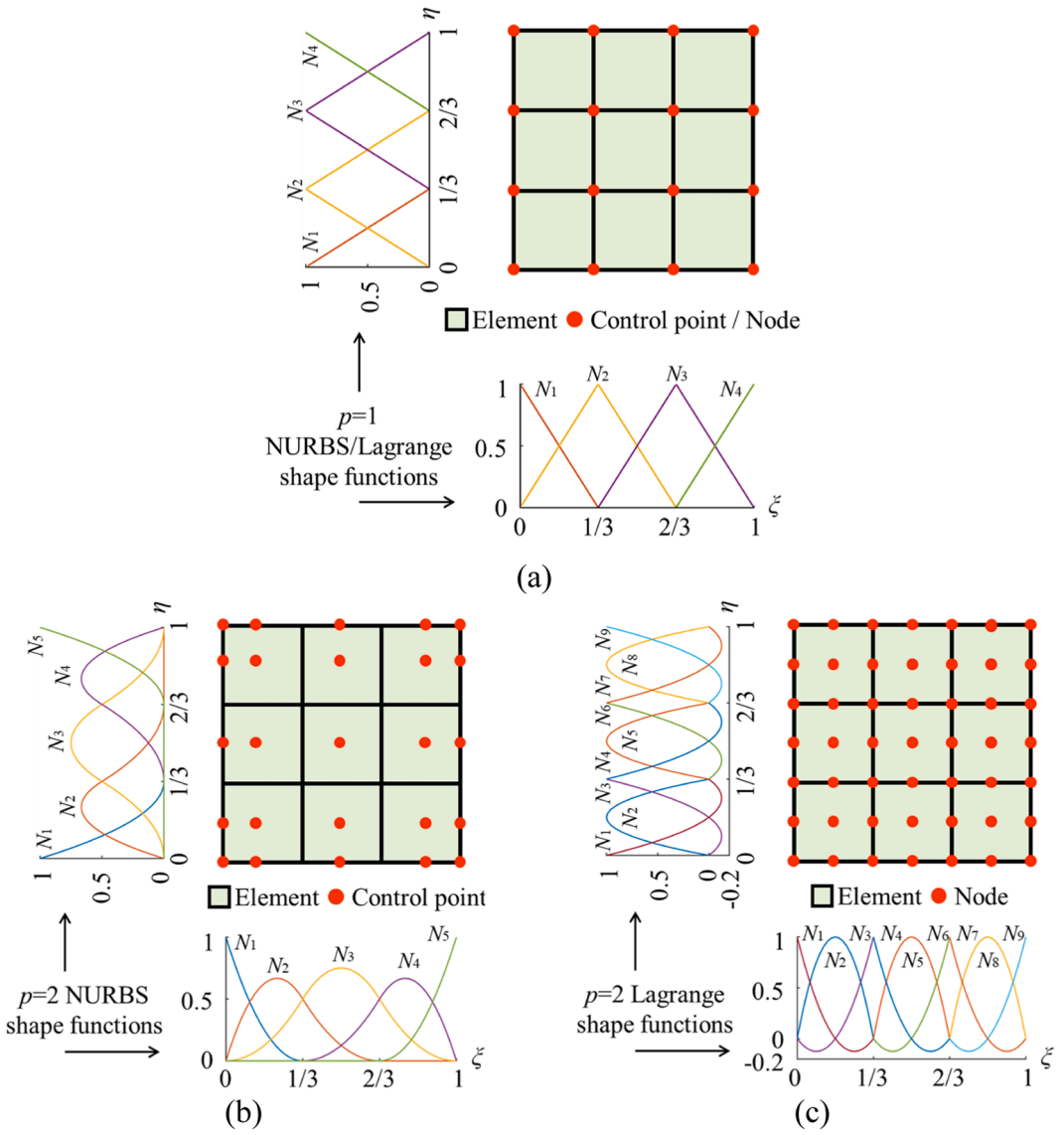


Fig. 1. Spatial discretization for a 2D plate: (a) Linear NURBS/Lagrange elements, (b) Quadratic NURBS elements of IGA, (c) Quadratic Lagrange elements of FEA.

$$S(\xi,\eta)=\sum_{i=1}^{n}\sum_{j=1}^{m}N_{i,p}^{j,q}(\xi,\eta)\boldsymbol{P}_{i,j} \tag{5}$$

where $\boldsymbol{P}_{i,j}$ is a control point on the NURBS surface.

2.2. Isogeometric structural mechanical analysis

Traditional FEA requires discretizing the analysis domain into elements, which introduces discrepancies between the discretized model and the original geometric model, thereby reducing accuracy. In contrast, IGA directly operates on an exact NURBS geometric model, eliminating spatial discretization errors [60]. Fig. 1 illustrates the 2D analysis domain after spatial discretization for both FEA and IGA, each comprising 3×3 elements. When using first-order elements ($p = 1$), the NURBS elements in IGA are identical to Lagrange elements, and the IGA control points align with the 16 nodes used in FEA. For quadratic elements ($p = 2$), the FEA model requires 49 nodes, whereas the IGA model only requires 25 control points, highlighting that IGA has significantly fewer degrees of freedom in higher-order cases compared to FEA. Additionally, IGA provides C^1 continuity between NURBS elements (see Fig. 1(b)), while FEA maintains only C^0 continuity between Lagrange elements (see Fig. 1(c)). The above analysis accuracy and advantages of IGA have been demonstrated in previous literature [84–86]. As a result, IGA ensures higher-order continuity of displacement and stress between elements, which is advantageous for structural fatigue analysis. Furthermore, we have included an example comparing IGA and FEA in Appendix A.

In IGA, the discrete static equilibrium equation for a linear elastic continuum can be given as:

$$\boldsymbol{KU}=\boldsymbol{F} \tag{6}$$

where $\boldsymbol{F}$ denotes the load vector, $\boldsymbol{U}$ is the global displacement vector, and $\boldsymbol{K}$ is the global stiffness matrix. The expressions for $\boldsymbol{U}$ and $\boldsymbol{K}$ are as follows [61,82]:

$$\boldsymbol{U}(\xi,\eta)=\sum_{i=1}^{m}\sum_{j=1}^{n}\boldsymbol{N}_{i,j}(\xi,\eta)\boldsymbol{u}_{i,j} \tag{7}$$

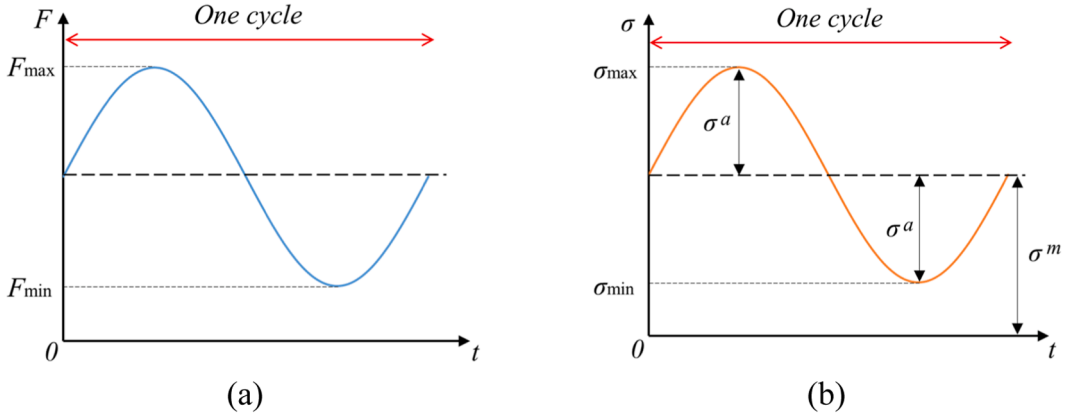


Fig. 2. A proportional cyclic load history: (a) Load, (b) Stress.

$$\begin{aligned}\boldsymbol{K} &= \sum_{e=1}^{NE} \boldsymbol{k}_e = \sum_{e=1}^{NE} \int_{\Omega_e} \boldsymbol{B}^T \boldsymbol{D}_0 \boldsymbol{B} d\Omega_e \\ &= \sum_{e=1}^{NE} \int_{\hat{\Omega}_e} \boldsymbol{B}^T \boldsymbol{D}_0 \boldsymbol{B} |\boldsymbol{J}_1| d\hat{\Omega}_e \\ &= \sum_{e=1}^{NE} \int_{\overline{\Omega}_e} \boldsymbol{B}^T \boldsymbol{D}_0 \boldsymbol{B} |\boldsymbol{J}_1||\boldsymbol{J}_2| d\overline{\Omega}_e\end{aligned} \tag{8}$$

where $\boldsymbol{u}_{i,j}$ denotes the displacement of the control point, $\boldsymbol{k}_e$ denotes the stiffness matrix of element e, NE is the total number of elements, $\boldsymbol{B}$ is the constitutive matrix, $\boldsymbol{D}_0$ is the stress-strain matrix, Ω_e and $\hat{\Omega}_e$ are the physical domain and the parameter domain of NURBS for element e, $\overline{\Omega}_e$ is the integral domain of element e, and $\boldsymbol{J}_1$ and $\boldsymbol{J}_2$ are the Jacobi transformation matrices from the NURBS parameter domain to the physical domain and from the integral domain to the NURBS parameter domain, respectively. Details of the specific equations have been provided in Appendix B.

For the 2D problem, the elemental stresses $\boldsymbol{\sigma}_e$ and von Mises stresses σ_e^{vm} based on the IGA are as follows:

$$\boldsymbol{\sigma}_e = \boldsymbol{D}_0 \boldsymbol{B} \boldsymbol{u}_e = \left[\sigma_{ex}, \sigma_{ey}, \tau_{exy}\right]^T \tag{9}$$

$$\sigma_e^{vm} = \sqrt{\left(\sigma_{ex}\right)^2 + \left(\sigma_{ey}\right)^2 - \sigma_{ex}\sigma_{ey} + 3\left(\tau_{exy}\right)^2} \tag{10}$$

where $\boldsymbol{u}_e$ is a displacement vector consisting of the control point displacements $\boldsymbol{u}_{i,j}$ of element e, and σ_{ex}, σ_{ey}, τ_{exy} are the three components of the stress vector of element e, respectively.

3. Structural fatigue analysis

This study focuses on ITO method under high-cycle fatigue constraints with constant amplitude. Therefore, this section primarily introduces the theoretical background related to proportional cyclic loading conditions and high-cycle fatigue failure (generally $\geq 10^7$ cycles), which form the basis for the FCITO method.

3.1. Proportional cyclic loading

The structural fatigue life is influenced by the stress amplitudes generated by cyclic loading. In this study, we focus on high-cycle fatigue under cyclic loading. Fig. 2(a) illustrates a proportional cyclic load, which induces a change in the stress state of the structure, as depicted in Fig. 2(b). The stress state of element e in the cyclic loading process can be defined as:

$$\sigma_e^a = \frac{(\sigma_e)_{\max} - (\sigma_e)_{\min}}{2} \tag{11}$$

$$\sigma_e^m = \frac{(\sigma_e)_{\max} + (\sigma_e)_{\min}}{2} \tag{12}$$

where σ_e^a is the stress amplitude, σ_e^m is the average stress, $(\sigma_e)_{\max}$ is the maximum stress under cyclic loading, and $(\sigma_e)_{\min}$ is the minimum stress under cyclic loading. It is important to note that stress amplitude and mean stress can be calculated from the maximum (or minimum) load by introducing appropriate scaling factors [31,32]. This method is applicable to cases where structures undergo elastic deformation under high-cycle fatigue. Therefore, the vectors of stress amplitude and mean stress are as follows:

$$\boldsymbol{\sigma}_e^a = c^a \boldsymbol{\sigma}_e = \left[\sigma_{ex}^a, \sigma_{ey}^a, \tau_{exy}^a\right]^T \tag{13}$$

$$\boldsymbol{\sigma}_e^m = c^m \boldsymbol{\sigma}_e = \left[\sigma_{ex}^m, \sigma_{ey}^m, \tau_{exy}^m\right]^T \tag{14}$$

Here, c^a and c^m are the scaling factors for stress amplitude and mean stress, respectively. Their expressions are as follows:

$$c^a = \frac{1 - (F_{\min}/F_{\max})}{2} \tag{15}$$

$$c^m = \frac{1 + (F_{\min}/F_{\max})}{2} \tag{16}$$

The von Mises stress measurement method is used to equivalently evaluate the stress amplitude and mean stress of the element as follows:

$$\sigma_e^{avm} = \sqrt{\left(\sigma_{ex}^a\right)^2 + \left(\sigma_{ey}^a\right)^2 - \sigma_{ex}^a\sigma_{ey}^a + 3\left(\tau_{exy}^a\right)^2} \tag{17}$$

$$\sigma_e^{mvm} = \sqrt{\left(\sigma_{ex}^m\right)^2 + \left(\sigma_{ey}^m\right)^2 - \sigma_{ex}\sigma_{ey} + 3\left(\tau_{exy}^m\right)^2} \tag{18}$$

where σ_e^{avm} and σ_e^{mvm} represent the equivalent stress amplitude and equivalent mean stress, respectively.

3.2. Fatigue theory

In the case of high-cycle fatigue, structural fatigue damage generally occurs at stress levels that do not exceed the yield stress. Currently, the mainstream theories for evaluating the uniaxial high-cycle fatigue damage of structures are the Gerber equation, the Goodman equation, the ASME-elliptic equation, and the Soderberg equation. The equations of the four theories are as follows [32,40,87]:

$$Gerber: D_e^{GB} = \frac{\sigma_e^a}{\sigma_{Nf}} + \left(\frac{\sigma_e^m}{\sigma_{ut}}\right)^2 \leq 1 \tag{19}$$

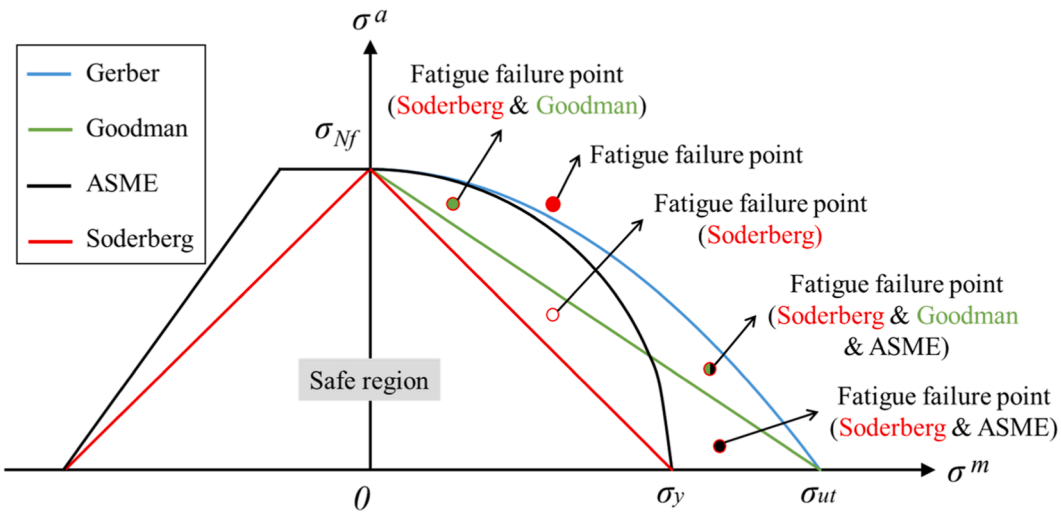


Fig. 3. Fatigue curves for Gerber, Goodman, ASME-elliptic, and Soderberg.

$$Goodman: D_e^{GM} = \frac{\sigma_e^a}{\sigma_{Nf}} + \frac{\sigma_e^m}{\sigma_{ut}} \le 1 \tag{20}$$

$$\text{ASME}-\text{elliptic}: D_e^{ASME} = \left(\frac{\sigma_e^a}{\sigma_{Nf}}\right)^2 + \left(\frac{\sigma_e^m}{\sigma_y}\right)^2 \le 1 \tag{21}$$

$$Soderberg: D_e^{SB} = \frac{\sigma_e^a}{\sigma_{Nf}} + \frac{\sigma_e^m}{\sigma_y} \le 1 \tag{22}$$

where σ_y denotes the yield stress, σ_{ut} denotes the ultimate stress, and σ_{Nf} represents the stress level at which a general metallic material will not fail under an infinite number of loading cycles. The stress σ_{Nf} can be calculated using the Basquin equation, which describes the S-N curve (S and N denote the stress and the load cycles when the structure fails respectively) [52]:

$$\sigma_{Nf} = \sigma_f'(2N_f)^b \tag{23}$$

where N_f denotes the number of load reversals, σ_f' denotes the fatigue strength coefficient, and b is fatigue strength exponent of the material.

The fatigue life curves corresponding to the four theories are illustrated in Fig. 3. It can be observed that the Soderberg equation is the most conservative of the four theories. In contrast, the other three theories allow for wider design domains, resulting in lower safety margins. Therefore, to account for all potential situations of damage, we select the Soderberg equation to evaluate damage generation in this study. The range defined by the combination of stress amplitude and mean stress that satisfies the conditions of the Soderberg equation is referred to as the safety region. In addition, when certain mechanical structures require a high safety factor, such as in aerospace and marine equipment, the conservative Soderberg equation is more appropriate. Building on the fatigue theories discussed above, the main objective of this paper is to solve the ITO problem subject to the Soderberg fatigue criterion. Also, the influence of compressive mean stress on structural damage is included in the optimization. In fact, metals are typically resistant to damage under compressive fatigue loading, as this type of loading does not promote crack propagation. Therefore, including compressive loads in the current study results in more conservative designs for metal structures.

4. Implementation of the FCITO method

In this section, we present a detailed description of the complete scheme of the FCITO method. First, the ITO model for fatigue damage constraints, along with the projection and filtering methods for the design variables, is described in Section 4.1. Subsequently, a material interpolation scheme based on the SIMP method is outlined in Section 4.2. Additionally, Section 4.3 illustrate the process of implementing fatigue constraints employing the modified P-norm function.

4.1. FCITO model

In this section, the topology optimization problem is defined as finding a structural design that maximizes stiffness while satisfying volume and fatigue constraints across the entire design domain. Therefore, we develop an ITO model for compliance minimization that satisfies the volume and fatigue constraints. The model is expressed as:

$$\begin{aligned} &\text{find}: \boldsymbol{\rho} \\ &\min: c(\boldsymbol{\rho}) = \boldsymbol{U}_1^{\mathrm{T}}\boldsymbol{K}\boldsymbol{U}_1 \\ &s.t. \begin{cases} \boldsymbol{K}\boldsymbol{U}_1 = \boldsymbol{F}_{\max},\ \boldsymbol{K}\boldsymbol{U}_2 = \boldsymbol{F}_{\min} \\ V(\boldsymbol{\rho}) = \sum_{e=1}^{NE} \rho_e v_e \le V_f \\ \max\left(D_e^{SB}\right) \le 1,\ e = 1,2,\cdots,NE \\ 0 < \rho_{\min} \le \rho_e^{i,j} \le 1,\ i = 1,2,\cdots,n;\ j = 1,2,\cdots,m \end{cases} \end{aligned} \tag{24}$$

where $V(\boldsymbol{\rho})$ denotes the total volume of the structure, v_e is the volume of the element e, $\boldsymbol{U}_1$ is the global displacement vector induced by the maximum load vector $\boldsymbol{F}_{\max}$, $\boldsymbol{U}_2$ is the global displacement vector induced by the minimum load vector $\boldsymbol{F}_{\min}$, V_f is the prescribed volume fraction, ρ_e denotes the relative density of element e, $\max\left(D_e^{SB}\right)$ denotes the maximum value of the structural damage, NE is the total number of elements, and $\rho_e^{i,j}$ denotes the relative density of the control points with element e, $\rho_{\min}$ is a small density used to avoid numerical singularities in the stiffness matrix (typical value $\rho_{\min} = 0.001$), n and m are the number of control points in the ξ and η directions, respectively. It is worth noting that the objective function aims to solve for the compliance minimization of the entire structure under the maximum load.

In the ITO, the element center density value is employed to represent the relative density of element ρ_e. This can be obtained by interpolating the NURBS basis functions of the control points with the following expression:

$$\rho_e = \sum_{i=1}^{n}\sum_{j=1}^{m} N_{i,p}^{j,q}\left(\xi_e^c, \eta_e^c\right)\widehat{\rho}_e^{i,j},\ \widehat{\rho}_e^{i,j} \in [0,1] \tag{25}$$

where (ξ_e^c, η_e^c) is the parametric coordinate of the center of element e, and $\widehat{\rho}_e^{i,j}$ is the density of control points after the projection associated with element e. The density is projected to reduce the gray scale elements in the optimization result. In this study, we project the filtered density field using the Heaviside projection function which is as follows [88]:

$$\widehat{\rho}_e^{i,j} = \frac{\tanh(\beta\alpha) + \tanh\left(\beta\left(\overline{\rho}_e^{i,j} - \alpha\right)\right)}{\tanh(\beta\alpha) + \tanh(\beta(1-\alpha))} \tag{26}$$

where $\overline{\rho}_e^{i,j}$ denotes the filtered density of the control point, β controls the curvature of the smoothed projection, and α defines the threshold that pushes the value of $\overline{\rho}_e^{i,j}$ to 0 or 1. In this work, we employ a single projection with $\alpha = 0.5$.

Furthermore, to avoid the checkerboard phenomenon during the optimization process and improve the computational efficiency, we adopt a density filter to solve the problem with the expression [89,90]:

$$\overline{\rho}_e^{i,j} = \frac{\sum\limits_{l \in N_{ij}} w_{ij,l}\left(\rho_e^{i,j}\right)_l}{\sum\limits_{la \in N_{ij}} w_{ij,la}} \tag{27}$$

$$w_{ij,l} = (r_{\min} - dist(ij,l)), \left\{l \in N_{ij} | dist(ij,l) \le r_{\min}\right\} \tag{28}$$

where $w_{ij,l}$ is the weight coefficient, N_{ij} is the total number of control points located within a certain radius distance from control point (i,j), $r_{\min}$ is the filtering radius, and $dist(ij,l)$ is the Euclidean distance between control points l and (i,j).

4.2. Material interpolation scheme based on SIMP method

The SIMP method is one of the most extensively utilized techniques in the field of topology optimization, owing to its remarkable generality and stability. Consequently, to accurately represent the relative density distribution within the design domain in ITO, we employ the SIMP method to define the relative density interpolation model for the material properties of the elements. The material interpolation scheme based on the SIMP method is as follows [9]:

$$E_e(\rho_e) = E_{\min} + (\rho_e)^{pp}(E_0 - E_{\min}) \tag{29}$$

where E_0 denotes the Young's modulus of the solid part of the material, while $E_{\min}$ represents a very small Young's modulus assigned to the cavity region to prevent singularities in the stiffness matrix. The parameter pp is a penalty factor, typically set to 3, to ensure a clear black-and-white solution.

According to the SIMP method, the interpolated global stiffness matrix $\boldsymbol{K}$ and objective function $c(\boldsymbol{\rho})$ are as follows:

$$\boldsymbol{K} = \sum_{e=1}^{NE} \boldsymbol{k}_e = \sum_{e=1}^{NE} E_e(\rho_e)\boldsymbol{k}_0 \tag{30}$$

$$c(\boldsymbol{\rho}) = \boldsymbol{U}_1^{\mathrm{T}}\boldsymbol{K}\boldsymbol{U}_1 = \sum_{e=1}^{NE} E_e(\rho_e)(\boldsymbol{u}_e)_1^{\mathrm{T}}\boldsymbol{k}_0(\boldsymbol{u}_e)_1 \tag{31}$$

where $\boldsymbol{k}_0$ represents the elemental stiffness matrix of the solid material in IGA, and $(\boldsymbol{u}_e)_1$ is the element displacement vector arising from the maximum load vector $\boldsymbol{F}_{\max}$.

4.3. Fatigue constraint

Similar to stress constraints, fatigue constraints are local measures and involve a substantial number of constraints in topology optimization [49,52,91]. Addressing this issue directly will be expensive. Therefore, we employ the P-norm function to address the fatigue damage constraint problem, aiming to mitigate the numerical burden resulting from the excessive number of constraints. The aggregation function for fatigue damage constraints is defined as follows:

$$D_{pn}^{SB} = \left(\sum_{e=1}^{NE}\left(D_e^{SB}\right)^{pn}\right)^{1/pn} \le 1 \tag{32}$$

where pn is the P-norm coefficient, typically set to 8. A higher value of pn yields more accurate calculations but may induce oscillations in the solution process. Conversely, a lower pn value results in less accurate calculations.

In this study, we adopt the normalized global stress measure method proposed by Le et al. [92], also known as adaptive constraint scaling [14]. This method leverages information from previous optimization iterations for scaling, enabling a closer approximation of the maximum stress. In this way, it effectively overcomes the limitations of the P-norm function in constraining the maximum stress. The damage obtained through the P-norm function is modified as follows:

$$\overline{D}_{pn}^{SB} \approx \chi^I D_{pn}^{SB} \le 1 \tag{33}$$

where χ^I is the scaling factor for the I-th iteration, and its expression is as follows:

$$\chi^I = \varphi^I \frac{\max\left(\left(D_e^{SB}\right)^{I-1}\right)}{\left(D_{pn}^{SB}\right)^{I-1}} + \left(1-\varphi^I\right)\chi^{I-1},\ \varphi^I \in (0,1] \tag{34}$$

where $\left(D_{pn}^{SB}\right)^{I-1}$ is the P-norm value of structural damage in the (I-1)-th iteration, and $\max\left(\left(D_e^{SB}\right)^{I-1}\right)$ denotes the maximum structural damage value in the (I-1)-th iteration. If oscillations occur in during the iterative process, a value of $0 < \varphi^I < 1$ is selected; otherwise, $\varphi^I = 1$ is chosen. As the iteration converges, $\left(D_{pn}^{SB}\right)^I \approx \left(D_{pn}^{SB}\right)^{I-1}$ and $\max\left(\left(D_e^{SB}\right)^I\right) \approx \max\left(\left(D_e^{SB}\right)^{I-1}\right)$, thereby achieving convergence, i.e. $\chi^I D_{pn}^{SB} \approx \max\left(\left(D_e^{SB}\right)^I\right)$. More details about this method can be found in reference [14,92].

In addition, fatigue optimization methods face the same challenges as stress optimization methods, such as singular solutions and nonlinear behavior. Therefore, we apply a relaxation method [93,94] to penalize Eq. (9) in order to address these issues. This method yields the stresses in element e as:

$$\overline{\boldsymbol{\sigma}}_e = \rho_e^{qq}\boldsymbol{D}_0\boldsymbol{B}_e(\boldsymbol{u}_e)_1 \tag{35}$$

where qq denotes the relaxation factor, with a typical value equal to 0.5.

5. Sensitivity analysis

To address the fatigue constraint problem using a gradient-based optimizer (e.g., MMA), it is necessary to derive the first-order sensitivity of the objective and constraint functions with respect to the design variable $\rho_e^{i,j}$. Since the sensitivities of the objective function and the volume constraint function with respect to the design variables have been extensively documented in other literature, we have included these fundamental equations in Appendix C and Appendix D. Therefore, this section focuses on elaborating the adjoint method for solving the sensitivity equations of the fatigue constraint function with respect to the design variables.

The first-order sensitivity of the fatigue constraint function to the design variable $\rho_e^{i,j}$ after processing utilizing the modified P-norm function is computed by the chain rule as:

Table 1
A typical mild steel material properties.

Material property	Value
Young's modulus E_0	210 GPa
Poisson's ratio υ	0.3
Fatigue strength coefficient $\sigma_f^{'}$	593 MPa
Fatigue strength exponent b	−0.086
The number of load reversals N_f	10^7
Yield stress σ_y	240 MPa
Ultimate stress σ_{ut}	358 MPa

Table 2
Parameters in ITO.

Parameter	Value
Order of NURBS basis functions	2
Young's modulus for void element $E_{\min}$	$10^{-9}E_0$
Density penalty factor pp	3
P-norm coefficient pn	8
Stress relaxation factor qq	0.5
Filtering radius $r_{\min}$	3
Maximum iteration step	200

$$\frac{\partial \overline{D}_{pn}^{SB}}{\partial \rho_e^{i,j}} = \frac{\partial \overline{D}_{pn}^{SB}}{\partial D_{pn}^{SB}} \frac{\partial D_{pn}^{SB}}{\partial D_e^{SB}} \left(\frac{\partial D_e^{SB}}{\partial \sigma_e^{avm}} \frac{\partial \sigma_e^{avm}}{\partial \boldsymbol{\sigma}_e^{a}} \frac{\partial \boldsymbol{\sigma}_e^{a}}{\partial \overline{\boldsymbol{\sigma}}_e} + \frac{\partial D_e^{SB}}{\partial \sigma_e^{mvm}} \frac{\partial \sigma_e^{mvm}}{\partial \boldsymbol{\sigma}_e^{m}} \frac{\partial \boldsymbol{\sigma}_e^{m}}{\partial \overline{\boldsymbol{\sigma}}_e} \right) \frac{\partial \overline{\boldsymbol{\sigma}}_e}{\partial \rho_e} \frac{\partial \rho_e}{\partial \widehat{\rho}_e^{i,j}} \frac{\partial \widehat{\rho}_e^{i,j}}{\partial \overline{\rho}_e^{i,j}} \frac{\partial \overline{\rho}_e^{i,j}}{\partial \rho_e^{i,j}} \tag{36}$$

Here, the expressions $\frac{\partial \overline{D}_{pn}^{SB}}{\partial D_{pn}^{SB}}$ and $\frac{\partial D_{pn}^{SB}}{\partial D_e^{SB}}$ are provided by Eqs. (33) and (32):

$$\frac{\partial \overline{D}_{pn}^{SB}}{\partial D_{pn}^{SB}} = \chi^I \tag{37}$$

$$\frac{\partial D_{pn}^{SB}}{\partial D_e^{SB}} = \left(\sum_{e=1}^{NE} \left(D_e^{SB} \right)^{pn} \right)^{1/pn-1} \left(D_e^{SB} \right)^{pn-1} \tag{38}$$

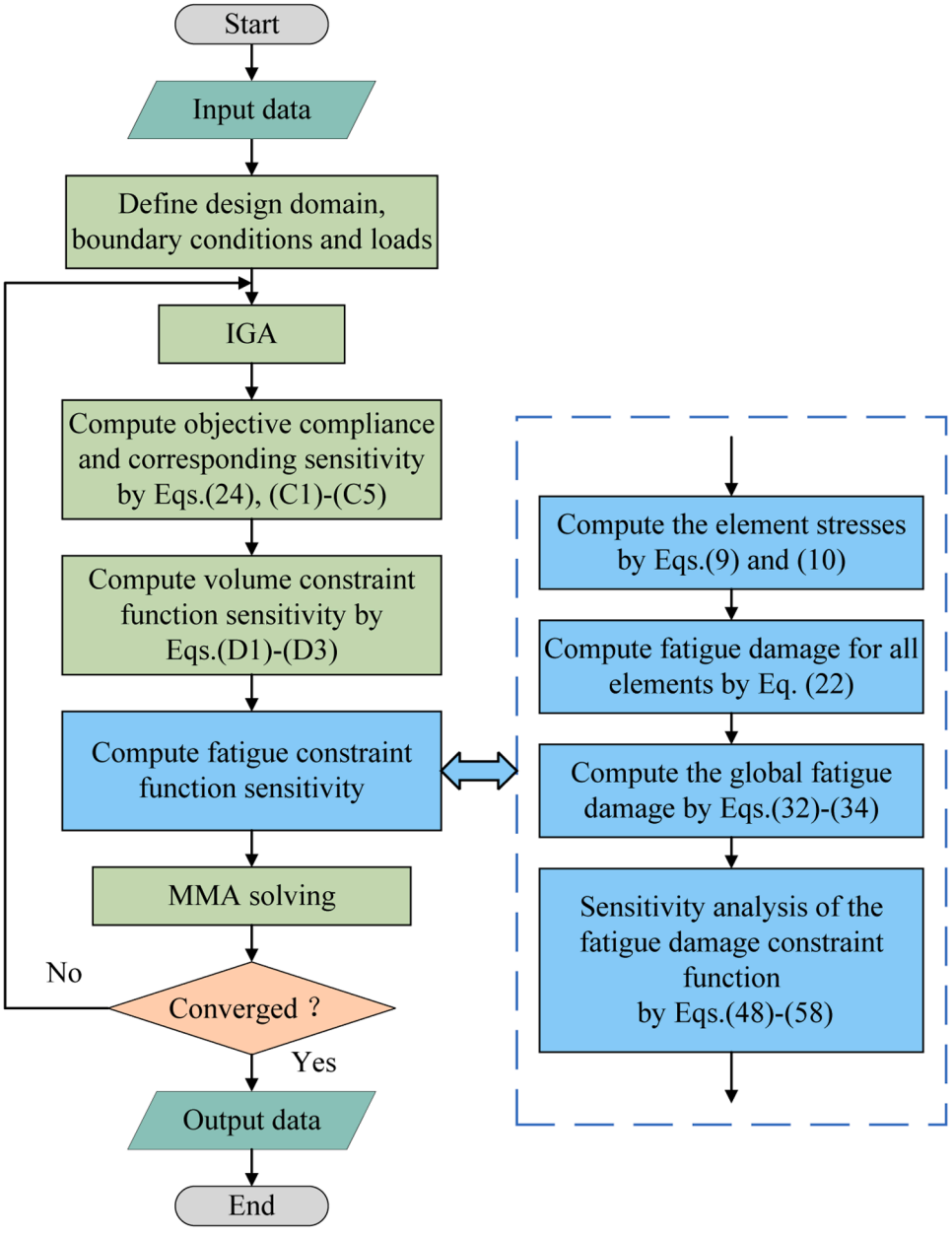


Fig. 4. The procedure flow chart of the presented FCITO method.

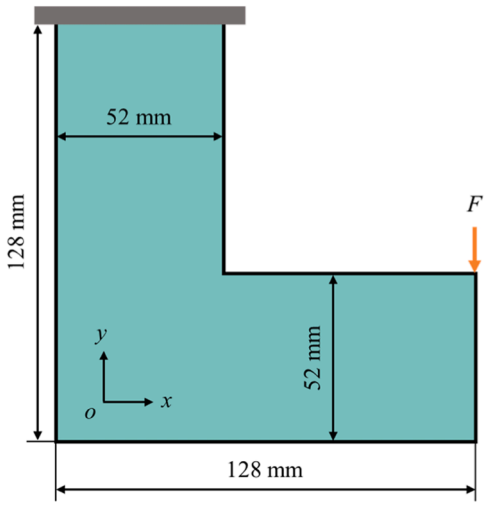


Fig. 5. The design domain and boundary conditions of the L-shaped bracket.

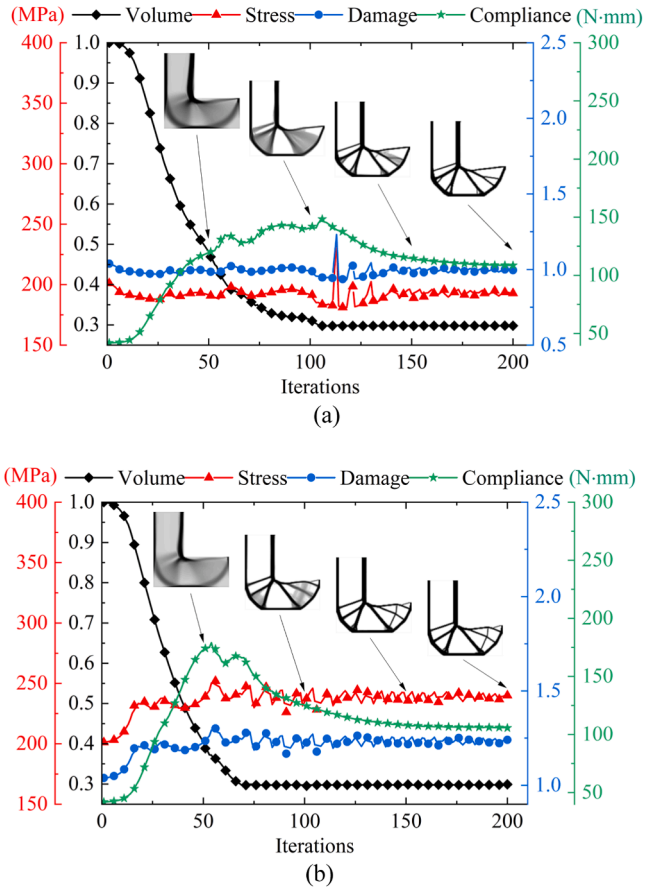


Fig. 6. Iterative histories of the L-shaped bracket: (a) FCITO method, (b) SCITO method.

The expressions $\frac{\partial D_e^{SB}}{\partial \sigma_e^{avm}}$ and $\frac{\partial D_e^{SB}}{\partial \sigma_e^{mvm}}$ are obtained according to Soderberg's equation:

$$\frac{\partial D_e^{SB}}{\partial \sigma_e^{avm}} = \frac{1}{\sigma_{Nf}} \tag{39}$$

$$\frac{\partial D_e^{SB}}{\partial \sigma_e^{mvm}} = \frac{1}{\sigma_y} \tag{40}$$

According to Eqs. (17) and (18), the expressions for $\frac{\partial \sigma_e^{avm}}{\partial \sigma_e^{a}}$ and $\frac{\partial \sigma_e^{mvm}}{\partial \sigma_e^{m}}$ are:

$$\frac{\partial \sigma_e^{avm}}{\partial \boldsymbol{\sigma}_e^{a}} = \frac{1}{2\sigma_e^{avm}} \begin{Bmatrix} 2\sigma_{ex}^{a} - \sigma_{ey}^{a} \\ 2\sigma_{ey}^{a} - \sigma_{ex}^{a} \\ 6\tau_{exy}^{a} \end{Bmatrix} \tag{41}$$

$$\frac{\partial \sigma_e^{mvm}}{\partial \boldsymbol{\sigma}_e^{m}} = \frac{1}{2\sigma_e^{mvm}} \begin{Bmatrix} 2\sigma_{ex}^{m} - \sigma_{ey}^{m} \\ 2\sigma_{ey}^{m} - \sigma_{ex}^{m} \\ 6\tau_{exy}^{m} \end{Bmatrix} \tag{42}$$

The expressions for $\frac{\partial \sigma_e^{a}}{\partial \overline{\sigma}_e}$ and $\frac{\partial \sigma_e^{m}}{\partial \overline{\sigma}_e}$ are derived from Eqs. (13) and (14), as follows:

$$\frac{\partial \boldsymbol{\sigma}_e^{a}}{\partial \overline{\boldsymbol{\sigma}}_e} = c^{a} \tag{43}$$

$$\frac{\partial \boldsymbol{\sigma}_e^{m}}{\partial \overline{\boldsymbol{\sigma}}_e} = c^{m} \tag{44}$$

According to Eqs. (9) and (35), the sensitivity $\frac{\partial \overline{\boldsymbol{\sigma}}_e}{\partial \rho_e}$ of the stresses to the element density has the following two components:

$$\frac{\partial \overline{\boldsymbol{\sigma}}_e}{\partial \rho_e} = qq\rho_e^{qq-1}\boldsymbol{D}_0\boldsymbol{B}_e(\boldsymbol{u}_e)_1 + \rho_e^{qq}\boldsymbol{D}_0\boldsymbol{B}_e\frac{\partial(\boldsymbol{u}_e)_1}{\partial \rho_e} \tag{45}$$

Here, since the expressions $\frac{\partial(\boldsymbol{u}_e)_1}{\partial \rho_e}$ is unknown. Therefore, we utilize the adjoint method to solve them and the following two equations can be obtained from the Eq. (6):

$$\frac{\partial \boldsymbol{k}_e}{\partial \rho_e}(\boldsymbol{u}_e)_1 + \boldsymbol{k}_e\frac{\partial(\boldsymbol{u}_e)_1}{\partial \rho_e} = \boldsymbol{0} \tag{46}$$

where $\frac{\partial \boldsymbol{k}_e}{\partial \rho_e}$ is derived according to Eqs. (29) and (30):

$$\frac{\partial \boldsymbol{k}_e}{\partial \rho_e} = (pp(\rho_e)^{pp-1}(E_0 - E_{\min}))\boldsymbol{k}_0 \tag{47}$$

Further, introducing the accompanying vectors $\boldsymbol{\lambda}_e^{a}$ and $\boldsymbol{\lambda}_e^{m}$ in Eq. (36) can be given:

$$\begin{aligned} \frac{\partial \overline{D}_{pn}^{SB}}{\partial \rho_e^{ij}} = \boldsymbol{A}_e \Bigg(& \boldsymbol{C}_e^{a}\left(qq\rho_e^{qq-1}\boldsymbol{D}_0\boldsymbol{B}_e(\boldsymbol{u}_e)_1 + \rho_e^{qq}\boldsymbol{D}_0\boldsymbol{B}_e\frac{\partial(\boldsymbol{u}_e)_1}{\partial \rho_e}\right) \\ & + (\boldsymbol{\lambda}_e^{a})^{T}\left(\boldsymbol{G}_e(\boldsymbol{u}_e)_1 + \boldsymbol{k}_e\frac{\partial(\boldsymbol{u}_e)_1}{\partial \rho_e}\right) \\ & + \boldsymbol{C}_e^{m}\left(qq\rho_e^{qq-1}\boldsymbol{D}_0\boldsymbol{B}_e(\boldsymbol{u}_e)_1 + \rho_e^{qq}\boldsymbol{D}_0\boldsymbol{B}_e\frac{\partial(\boldsymbol{u}_e)_1}{\partial \rho_e}\right) \\ & + (\boldsymbol{\lambda}_e^{m})^{T}\left(\boldsymbol{G}_e(\boldsymbol{u}_e)_1 + \boldsymbol{k}_e\frac{\partial(\boldsymbol{u}_e)_1}{\partial \rho_e}\right)\Bigg)\boldsymbol{H}_e \end{aligned} \tag{48}$$

where $\boldsymbol{A}_e$, $\boldsymbol{C}_e^{a}$, $\boldsymbol{C}_e^{m}$, $\boldsymbol{G}_e$ and $\boldsymbol{H}_e$ are expressions as follows:

$$\boldsymbol{A}_e = \chi^{I}\left(\sum_{e=1}^{NE}(D_e^{SB})^{pn}\right)^{1/pn-1}(D_e^{SB})^{pn-1} \tag{49}$$

$$\boldsymbol{C}_e^{a} = c^{a}\frac{1}{\sigma_{Nf}}\frac{1}{2\sigma_e^{avm}}\begin{Bmatrix} 2\sigma_{ex}^{a} - \sigma_{ey}^{a} \\ 2\sigma_{ey}^{a} - \sigma_{ex}^{a} \\ 6\tau_{exy}^{a} \end{Bmatrix} \tag{50}$$

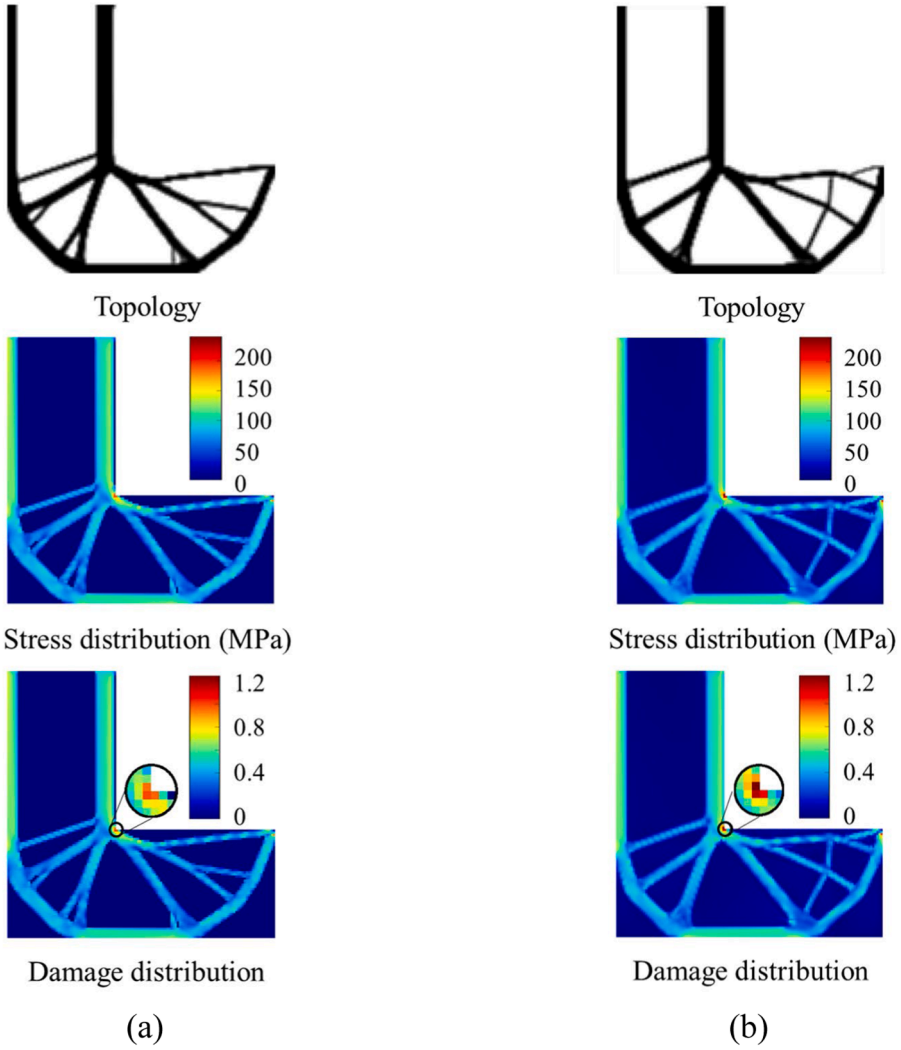


Fig. 7. Optimization results of the L-shaped bracket: (a) FCITO method, (b) SCITO method.

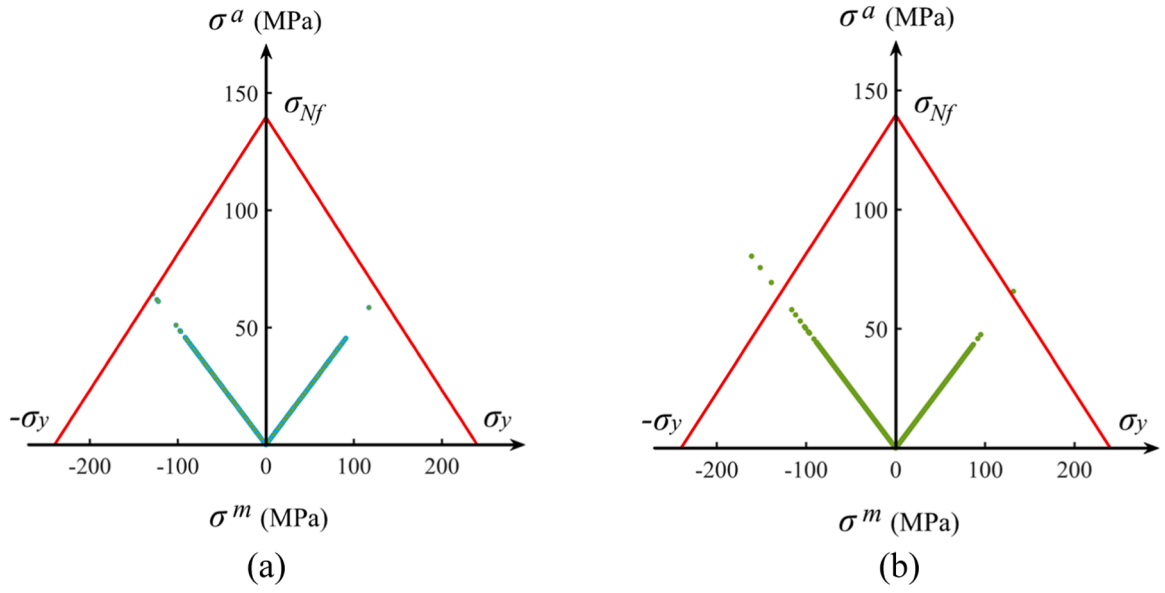


Fig. 8. Soderberg diagrams of the L-shaped bracket damage: (a) FCITO method, (b) SCITO method.

Table 3
The compliance, maximum stress, and maximum damage of the L-shaped bracket from different methods.

Method	Compliance (N·mm)	Max. stress (MPa)	Max. damage
FCITO	108.53	192.84	0.996
SCITO	105.55	240.00	1.241

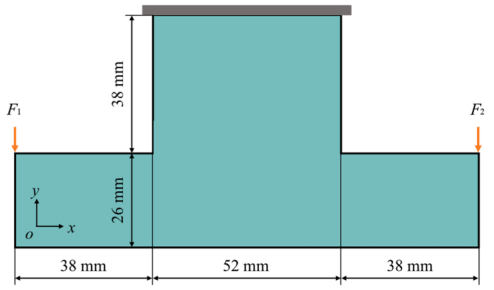


Fig. 9. The design domain and boundary conditions of the double L-shaped bracket.

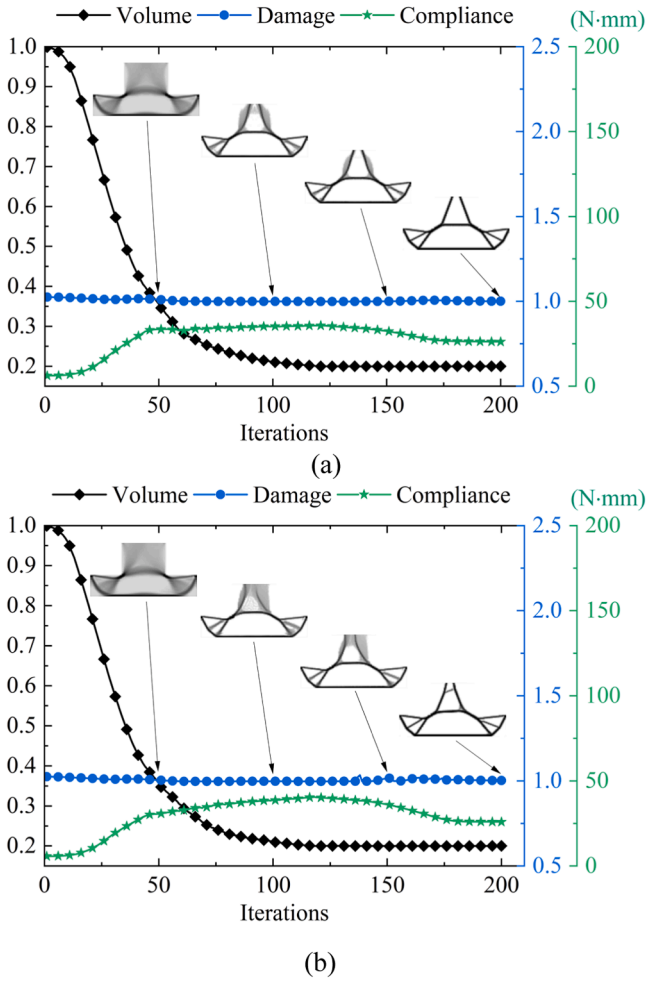


Fig. 10. Iterative histories of the double L-shaped bracket: (a) Load case 1, (b) Load case 2.

$$\boldsymbol{C}_e^{\mathrm{m}} = c^m \frac{1}{\sigma_y} \frac{1}{2\sigma_e^{mvm}} \begin{Bmatrix} 2\sigma_{ex}^m - \sigma_{ey}^m \\ 2\sigma_{ey}^m - \sigma_{ex}^m \\ 6\tau_{exy}^m \end{Bmatrix} \tag{51}$$

$$\boldsymbol{G}_e = \left(pp(\rho_e)^{pp-1}(E_0 - E_{\min})\right)\boldsymbol{k}_0 \tag{52}$$

$$\boldsymbol{H}_e = \sum_{i=1}^{n}\sum_{j=1}^{m} N_{i,p}^{j,q}(\xi_e,\eta_e) \frac{\beta\left(\operatorname{sech}\left(\beta\left(\overline{\rho}_e^{i,j} - \alpha\right)\right)\right)^2}{\tanh(\beta\alpha) + \tanh(\beta(1-\alpha))} \frac{\boldsymbol{w}_{ij,l}}{\sum_{la\in N_{ij}} \boldsymbol{w}_{ij,la}} \tag{53}$$

For removing the unknown expression $\frac{\partial(\boldsymbol{u}_e)_1}{\partial\rho_e}$, the following method is employed to solve for the accompanying vectors $\boldsymbol{\lambda}_e^a$ and $\boldsymbol{\lambda}_e^{\mathrm{m}}$.

$$\boldsymbol{C}_e^a \rho_e^{qq} \boldsymbol{D}_0 \boldsymbol{B}_e + \left(\boldsymbol{\lambda}_e^a\right)^T \boldsymbol{k}_e = \boldsymbol{0} \tag{54}$$

$$\boldsymbol{C}_e^{\mathrm{m}} \rho_e^{qq} \boldsymbol{D}_0 \boldsymbol{B}_e + \left(\boldsymbol{\lambda}_e^{\mathrm{m}}\right)^T \boldsymbol{k}_e = \boldsymbol{0} \tag{55}$$

Therefore, the equations for the accompanying vectors $\boldsymbol{\lambda}_e^a$ and $\boldsymbol{\lambda}_e^m$ can be obtained as follows:

$$\boldsymbol{\lambda}_e^a = \left(-\boldsymbol{C}_e^a \rho_e^{qq} \boldsymbol{D}_0 \boldsymbol{B}_e \boldsymbol{k}_e^{-1}\right)^T \tag{56}$$

$$\boldsymbol{\lambda}_e^{\mathrm{m}} = \left(-\boldsymbol{C}_e^{\mathrm{m}} \rho_e^{qq} \boldsymbol{D}_0 \boldsymbol{B}_e \boldsymbol{k}_e^{-1}\right)^T \tag{57}$$

Finally, we gained an expression for the sensitivity of the fatigue constraint function after treatment with the modified P-norm function:

$$\begin{aligned} \frac{\partial \overline{D}_{pn}^{SB}}{\partial \rho_e^{i,j}} = \boldsymbol{A}_e \Big(& \boldsymbol{C}_e^a qq \rho_e^{qq-1} \boldsymbol{D}_0 \boldsymbol{B}_e (\boldsymbol{u}_e)_1 + \left(\boldsymbol{\lambda}_e^a\right)^T \boldsymbol{G}_e (\boldsymbol{u}_e)_1 \\ & + \boldsymbol{C}_e^{\mathrm{m}} qq \rho_e^{qq-1} \boldsymbol{D}_0 \boldsymbol{B}_e (\boldsymbol{u}_e)_1 + \left(\boldsymbol{\lambda}_e^{\mathrm{m}}\right)^T \boldsymbol{G}_e (\boldsymbol{u}_e)_1 \Big) \boldsymbol{H}_e \end{aligned} \tag{58}$$

6. Numerical examples and discussion

In this section, we demonstrate the effectiveness of the FCITO method through several examples. All examples utilize the properties of typical mild steel, with the relevant parameters provided in Table 1 [31]. The procedure flow chart of the presented FCITO method is shown in Fig. 4. For high-cycle fatigue problems, the stresses induced by external loads typically remain well below the structural strength limit and predominantly result in elastic deformations. Thus, we assume that the material is isotropic and linear elastic. Simultaneously, the design domain of the 2D structures is discretized applying quadratic NURBS quadrilateral elements, while the 3D structures are discretized applying quadratic NURBS hexahedral elements. The initial density variable of the elements is set to 1, with the move limit for the MMA asymptotes set to 0.02 for 2D structures and 0.25 for 3D structures to ensure stable optimization iterations. The relevant parameters in the ITO are provided in Table 2. Additionally, all examples were computed on a desktop PC equipped with a CPU Inter® Core™ i7–12700F of 2.1 GHz, 12 cores, 20 threads, 32 GB of RAM, and implemented using MATLAB®2022a software.

6.1. Example 1: L-shaped bracket

In the first example, the validity of the FCITO method was verified utilizing a classical L-shaped bracket. The structural dimensions, boundary conditions, and applied loads for this L-shaped bracket are described in Fig. 5. The design domain is discretized adopting 10,608 quadratic NURBS quadrilateral elements. The high-cycle fatigue loads applied to the structure have a maximum magnitude of $F_{\max} = 270N$ and

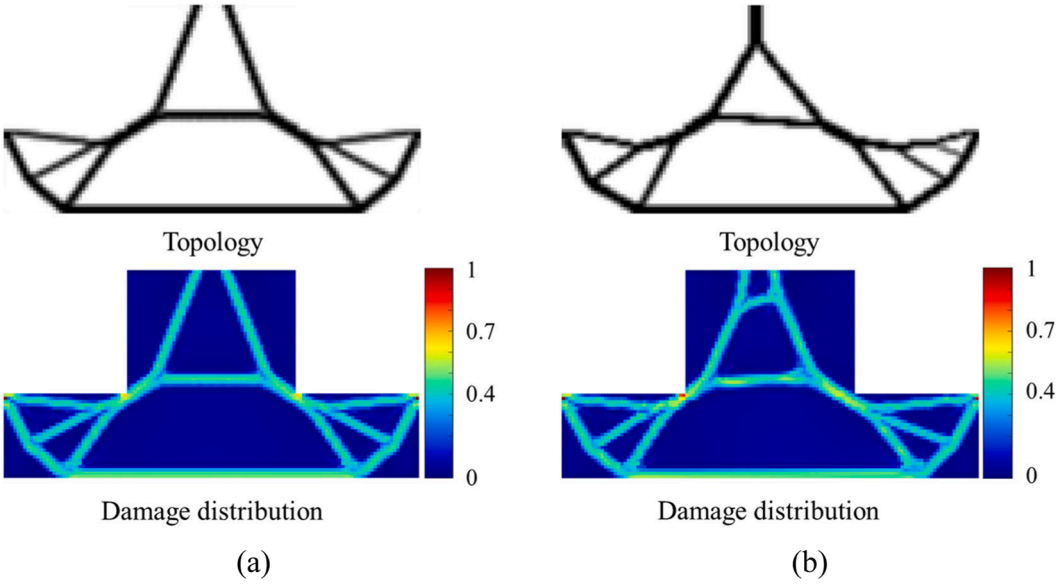


Fig. 11. Optimization results of the double L-shaped bracket: (a) Load case 1, (b) Load case 2.

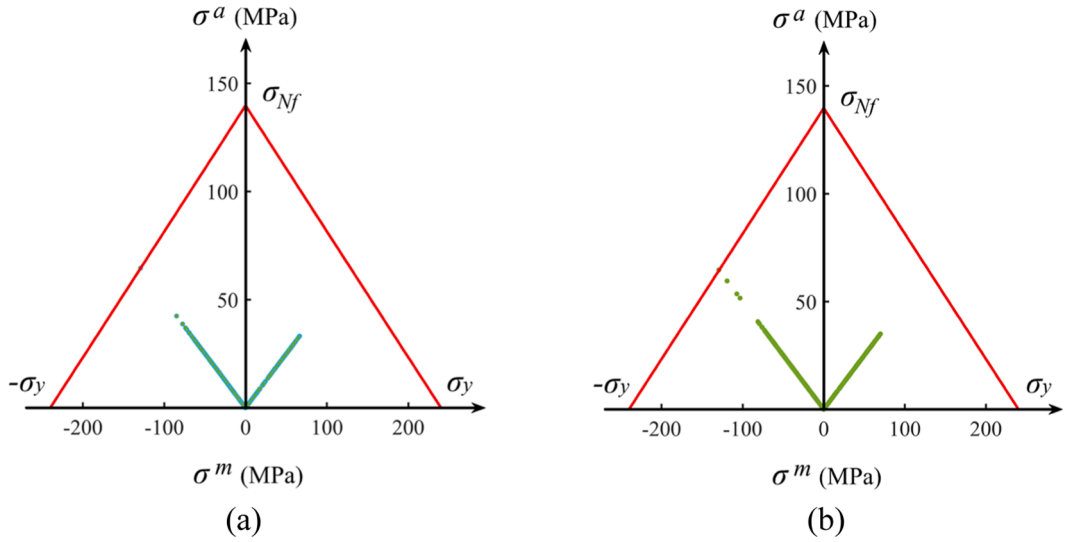


Fig. 12. Soderberg diagrams of the double L-shaped bracket damage: (a) Load case 1, (b) Load case 2.

Table 4
The compliance, maximum stress, and maximum damage of the double L-shaped bracket under different load cases.

Load	Compliance (N·mm)	Max. damage
Case 1	26.20	1.000
Case 2	25.94	1.000

a minimum magnitude of $F_{\min} = 90N$. Additionally, the L-shaped bracket is subjected to a volume fraction of $V_f = 0.3$ during the optimization process.

To validate the effectiveness of the proposed FCITO method, we employ a traditional stress-constrained isogeometric topology optimization (SCITO) method for comparison. It is important to note that the SCITO method is applied to the minimum compliance problem under volume and stress constraints, where the volume constraint is set to $V_f = 0.3$ and the stress constraint is set to $\sigma_y = 240$MPa. In this study, the parameter settings for both methods are kept consistent. Fig. 6 exhibits the iterative histories of the optimization process for the L-shaped bracket using both the FCITO and SCITO methods. The resulting topologies for the L-shaped bracket, obtained through these two methods, are displayed in Fig. 7, revealing their differences in structural layout. Furthermore, Fig. 8 illustrates the Soderberg diagrams of the L-shaped bracket damage, offering a detailed view of the fatigue characteristics observed in the structure. Notably, the topologies generated by both methods exhibit a specific curvature at the corners, aimed at mitigating excessive stress concentration in these regions. It is also evident that the topologies differ between the two methods. The results show that the combination of stress amplitude and mean stress in the topology generated by the FCITO method lies within the safe region of the Soderberg diagram. This indicates that the final structural design is fatigue-resistant under the specified number of reversals ($N_f = 10^7$). In contrast, the topology obtained using the traditional SCITO method exceeds the safe limits allowed by the Soderberg criterion (outside the safe region). These results demonstrate that, under the same volume constraint, the topology generated by the FCITO method satisfies the fatigue damage criterion constraints.

Additionally, Table 3 gives the compliance, maximum stress, and

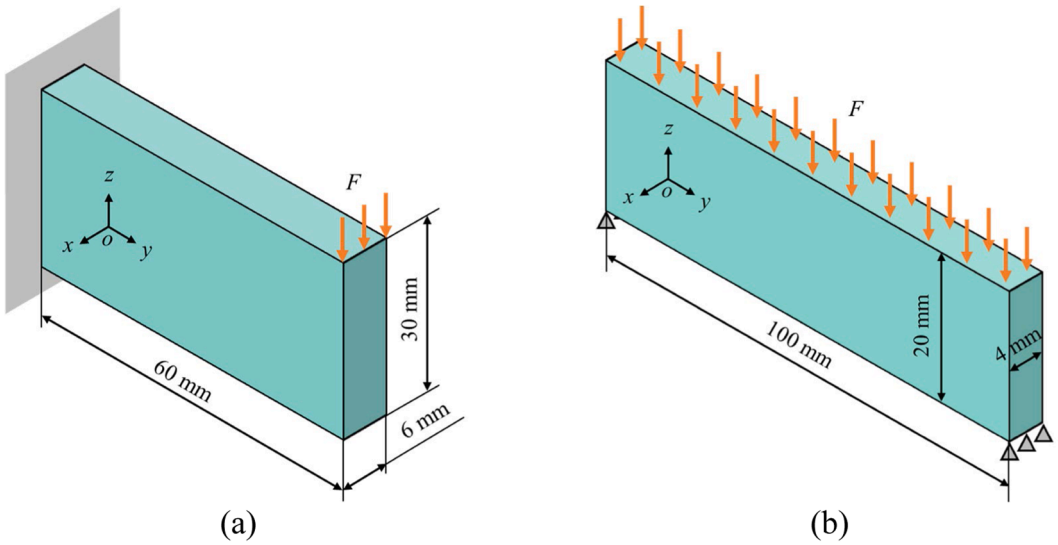


Fig. 13. The 3D models: (a) 3D cantilever beam, (b) 3D bridge.

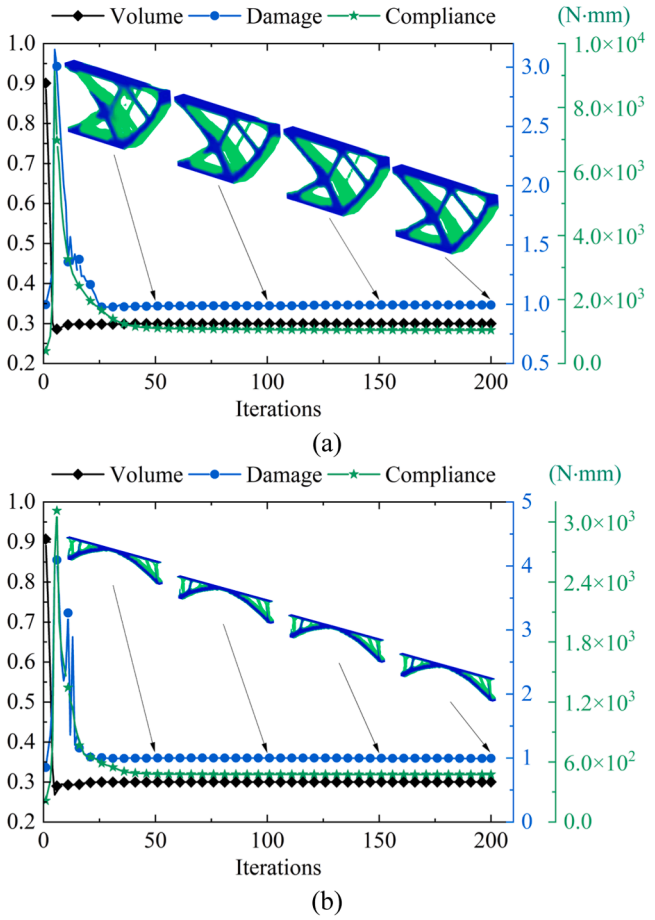


Fig. 14. Iterative histories of the two 3D models: (a) 3D cantilever beam, (b) 3D bridge.

maximum damage for the two designs of the L-shaped bracket. The compliance values obtained by the two methods are similar, with the FCITO method yielding slightly higher values. The maximum stress obtained by the SCITO method is equal the yield stress threshold of σ_y = 240MPa, while the maximum damage reaches 1.241, and the compliance is 105.55 N·mm. Compared to the SCITO method, the L-shaped bracket structure optimized by the FCITO method satisfies the fatigue constraints while reducing maximum stress by 19.65 %, with a 2.82 % increase in compliance. This demonstrates that the FCITO method significantly mitigates stress concentration at the bending edges, thereby preventing fatigue damage.

6.2. *Example 2: double L-shaped bracket*

In the second example, we adopted a double L-shaped bracket to discuss the effects of symmetric and asymmetric loads on the optimization results of the FCITO method. Note that the FCITO method does not account for stress constraints. The design domain, boundary conditions, and applied loads for this double L-shaped bracket are depicted in Fig. 9. The double L-shaped bracket was discretized applying 5304 quadratic NURBS quadrilateral elements and the volume fraction was set to 0.2 during the optimization process. Under symmetric loading conditions (named load case 1), the high-cycle fatigue load has a maximum magnitude of $(F_1)_{\max} = (F_2)_{\max} = 120N$ and a minimum magnitude of $(F_1)_{\min} = (F_2)_{\min} = 40N$. For asymmetric loading (named load case 2), the maximum magnitude and minimum magnitude of the high-cycle fatigue load F_1 are $(F_1)_{\max} = 120N$ and $(F_1)_{\min} = 40N$, respectively, and the maximum magnitude and minimum magnitude of the high-cycle fatigue load F_2 are $(F_2)_{\max} = 110N$ and $(F_2)_{\min} = 36N$, respectively.

The iteration histories for optimizing the double L-shaped bracket using the FCITO method under different loading conditions are shown in Fig. 10. Approximately 175 iterations are required to achieve steady-state convergence for both cases. Fig. 11 presents the resulting topologies for both load cases, along with the corresponding stress and fatigue damage distributions. The analysis indicates that the optimized topology is symmetric when symmetric high-cycle fatigue loads are applied on both sides of the structure. However, under asymmetric high-cycle fatigue loads, the resulting topology exhibits noticeable asymmetry. Additionally, Fig. 12 shows Soderberg diagrams of the double L-shaped bracket damage. The combinations of stress amplitude and mean stress in the topologies obtained under both load cases are located within the safe region of the Soderberg diagram.

Table 4 provides the compliance, maximum stress, and maximum damage values for the double L-shaped bracket under different load cases. In load case 1, the optimized bracket has a maximum compliance of 26.20 N·mm and a maximum damage value of 1.000. In load case 2, the maximum compliance is 25.94 N·mm and the maximum damage is 1.000. These results demonstrate that the FCITO method effectively

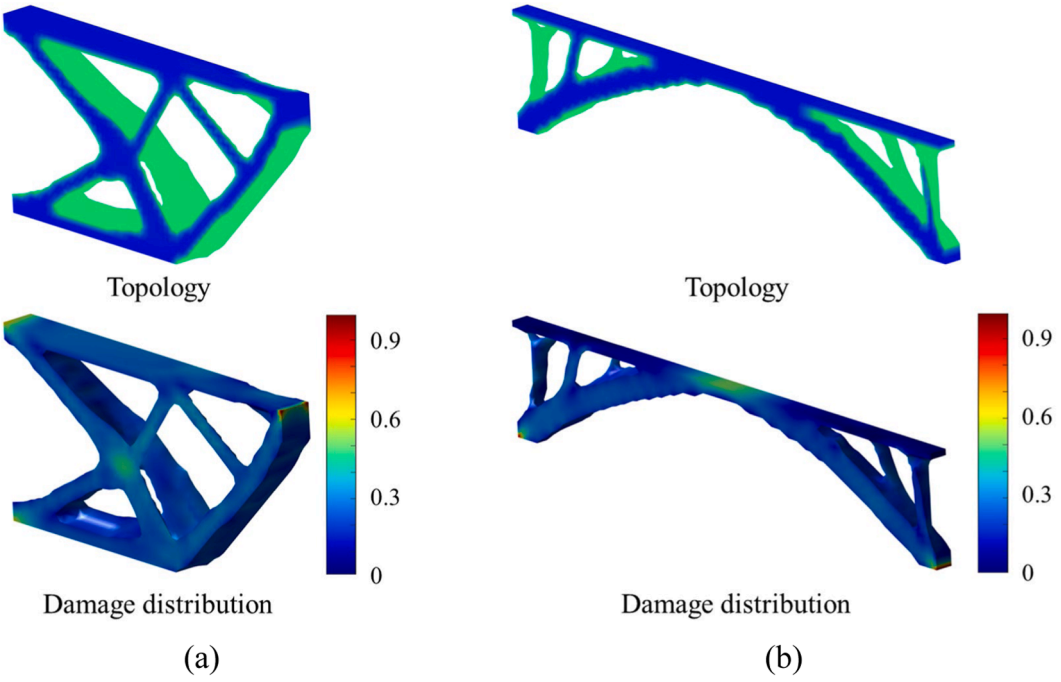


Fig. 15. Optimization results of the two 3D models: (a) 3D cantilever beam, (b) 3D bridge.

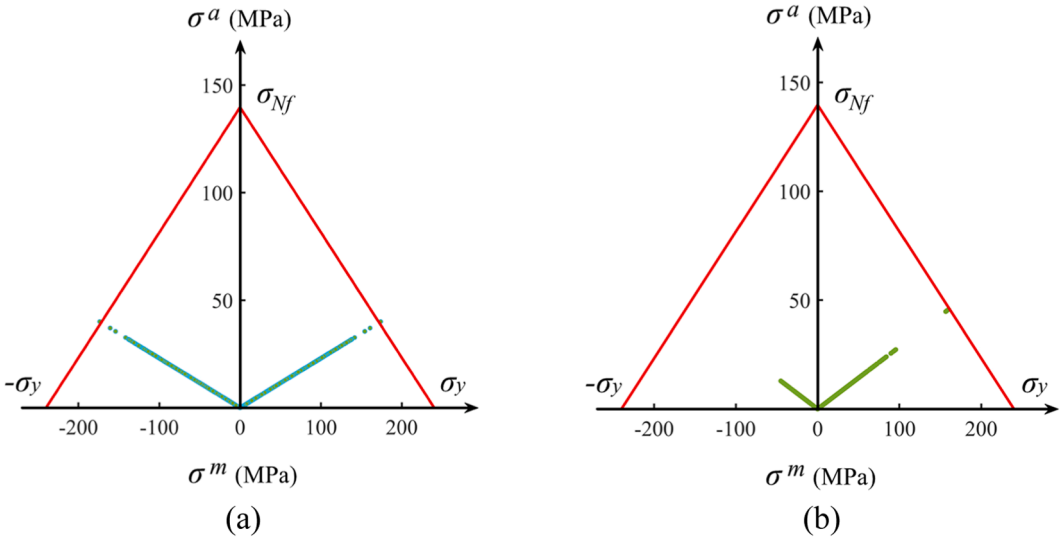


Fig. 16. Soderberg diagrams of damage for the two 3D models: (a) 3D cantilever beam, (b) 3D bridge.

Table 5
The compliance, maximum stress, and maximum damage of the two 3D models.

Model	Compliance (N·mm)	Max. damage
3D cantilever beam	1043.63	0.993
3D bridge	474.81	0.994

limits maximum fatigue damage under both symmetric and asymmetric loading. Additionally, the findings reveal that asymmetric loading results in higher stress levels, likely due to stress concentration effects associated with asymmetric load distribution.

6.3. Example 3: 3D model

In this section, two 3D models are employed to verify the feasibility of the FCITO method for addressing 3D problems. The FCITO method, which does not take into account the stress constraints, is applied in the optimization of the two 3D models. The geometry, boundary conditions, and loading conditions for both 3D models are illustrated in Fig. 13. The 3D cantilever beam and 3D bridge are discretized by 10,800 and 8000 quadratic NURBS hexahedral elements, respectively. For these two 3D structural design domains, the volume fraction and the number of load reversals are set to the same values, 0.3 and 10^7, respectively. The high-cycle fatigue load, uniformly applied to the top right boundary of the 3D cantilever beam, has a maximum value of $F_{\max} = 608N$ and a minimum value of $F_{\min} = 320N$. Similarly, the high-cycle fatigue load, uniformly distributed across the top of the 3D bridge structure, has a maximum value of $F_{\max} = 1101.6N$ and a minimum value of $F_{\min} = 612N$.

Fig. 14 depicts the iteration histories of the 3D cantilever beam and 3D bridge obtained employing the FCITO method. It can be observed that the two 3D structural designs converge to a stabilized state after

about 50 iterations. The optimization results for these structures are presented in Fig. 15, while the corresponding Soderberg diagrams are displayed in Fig. 16. Table 5 provides a detailed summary of the compliance, maximum stress, and maximum damage for both designs. The optimized 3D cantilever beam achieves a maximum compliance of 1043.63 N·mm and the maximum damage value of 0.993. For the optimized 3D bridge, the maximum compliance is 474.81 N·mm and the maximum damage is 0.994. These results indicate that the maximum damage of both the 3D cantilever beam and the 3D bridge has been effectively controlled, demonstrating the feasibility of the proposed FCITO method for fatigue-resistant optimization of 3D structures.

6.4. Discussion

The presented FCITO method has been demonstrated using the example of an L-shaped bracket, showing its ability to constrain the Soderberg fatigue criterion below a threshold value. This indicates that the optimized structure will not experience fatigue failure under the specified number of load reversals. Furthermore, the FCITO method has been validated in addressing the fatigue design problem of 3D structures through examples of a 3D cantilever beam and a 3D bridge. However, the proposed FCITO method still has certain limitations and requires further investigation.

Firstly, the FCITO method does not account for more complex multiaxial fatigue criteria, such as the Sines, Crossland, and Findley criteria [38]. In future work, the FCITO method could be extended to address more complex multiaxial fatigue damage and non-proportional loading problems, thereby enabling structural optimization under more challenging loading conditions.

Secondly, more advanced aggregation methods could be employed to better approximate maximum fatigue damage, such as the maximum rectifier function [14]. Additionally, the augmented Lagrangian method could be considered to achieve more precise control over local constraints [37].

Thirdly, material plastic deformation could be incorporated into the FCITO method, making the theoretical model more closely aligned with real-world engineering applications.

7. Conclusions

In this work, we present an ITO method based on the SIMP method, incorporating fatigue constraints, and develop the corresponding mathematical model. The method aims to minimize structural compliance while accounting for volume and fatigue constraints. The FCITO method specifically addresses the high-cycle fatigue problem of structures under proportional cyclic loading, leveraging the higher-order continuity of IGA elements to enhance analytical accuracy. To manage challenges such as the large number of constraints of fatigue problems, the modified P-norm function is employed to approximate the maximum fatigue damage of the elements with high precision, yielding a functional form suitable for gradient-based optimization methods. Meanwhile, the relaxation method is utilized to address singularity issues. The sensitivity equations for the fatigue constraint function with respect to the design variables are derived using the adjoint method. Additionally, the proposed FCITO method is compared to the conventional SCITO method using an L-shaped bracket as test example. The FCITO method demonstrates superior effectiveness in mitigating structural fatigue damage compared to the SCITO method under equivalent material volume conditions. Notably, the optimized L-shaped bracket applying the FCITO method achieves a 19.65 % reduction in maximum stress, with only a 2.82 % increase in compliance. Furthermore, the effects of symmetric and asymmetric loading on the optimization results are analyzed using a double L-shaped bracket as an example. To further evaluate the feasibility and effectiveness of the FCITO method in solving high-cycle fatigue optimization for 3D structures, two 3D examples (a 3D cantilever beam and a 3D bridge structure) are presented. These examples demonstrate that the FCITO method can successfully limit fatigue damage while achieving lightweight structural design.

CRediT authorship contribution statement

Jinyu Gu: Writing – original draft, Software, Methodology, Investigation, Conceptualization. **Jianghong Yang:** Software, Resources. **Yingjun Wang:** Writing – review & editing, Supervision, Funding acquisition.

Declaration of competing interest

The authors declare that they have no known competing financial interests or personal relationships that could have appeared to influence the work reported in this paper.

Acknowledgments

This work has been supported by the Guangdong Basic and Applied Basic Research Foundation (2024A1515011786) and National Natural Science Foundation of China (52075184).

Appendix A. A simple example of IGA and FEA comparison

In this example, a simple 2D plate structure is employed to demonstrate the advantages of the IGA method over the traditional FEA method. The boundary conditions for the 2D plate are illustrated in Fig. A1. The left boundary is fixed, while a uniformly distributed static load of $F = 10N/\text{mm}$ is applied at the right boundary. As shown in Fig. A2, IGA contains 512 quadratic NURBS elements and FEA contains 2048 quadratic Lagrange elements. The IGA method employs 612 control points (1224 degrees of freedom), while the FEA method uses 8385 nodes (16,770 degrees of freedom). It is worth noting that the FEA analysis results were computed using commercial software and processed in MATLAB.

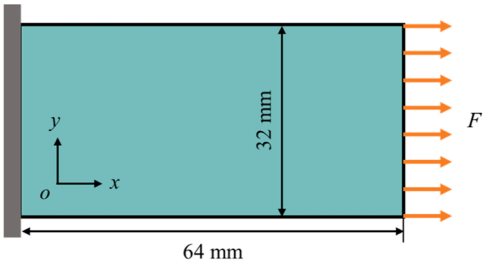


Fig. A1. The boundary conditions of the 2D plate.

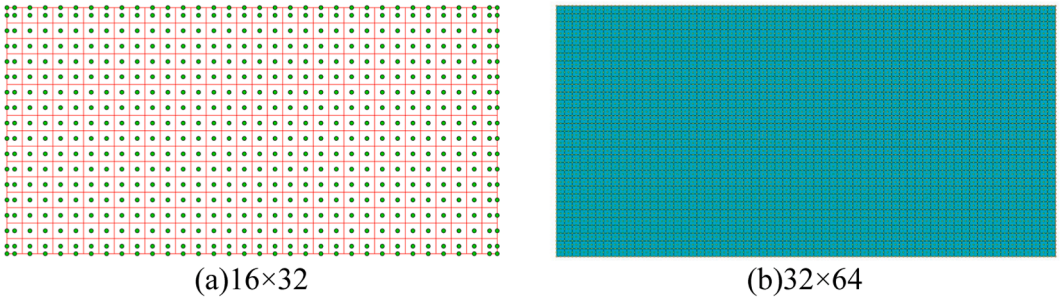


Fig. A2. Mesh for the 2D plate: (a) IGA, (b) FEA.

Fig. A3 displays the displacement results for the 2D plate. It can be observed that the displacement results obtained using IGA closely align with those from FEA. Fig. A4 illustrates the stress results for the 2D plate, further demonstrating that the IGA analysis results are in good agreement with those from FEA. These results demonstrate that IGA can achieve higher analytical accuracy with fewer elements and degrees of freedom. The reduced number of degrees of freedom decreases the size of the stiffness matrix, thereby enhancing the efficiency of solving the system of equilibrium equations. It should be noted that this simple example was used to illustrate the advantages of IGA, without delving into an in-depth analysis. The primary focus of this study is to develop a topology optimization method for high-cycle fatigue utilizing the IGA framework. A more comprehensive discussion of the benefits of IGA can be found in the literature [84–86,95].

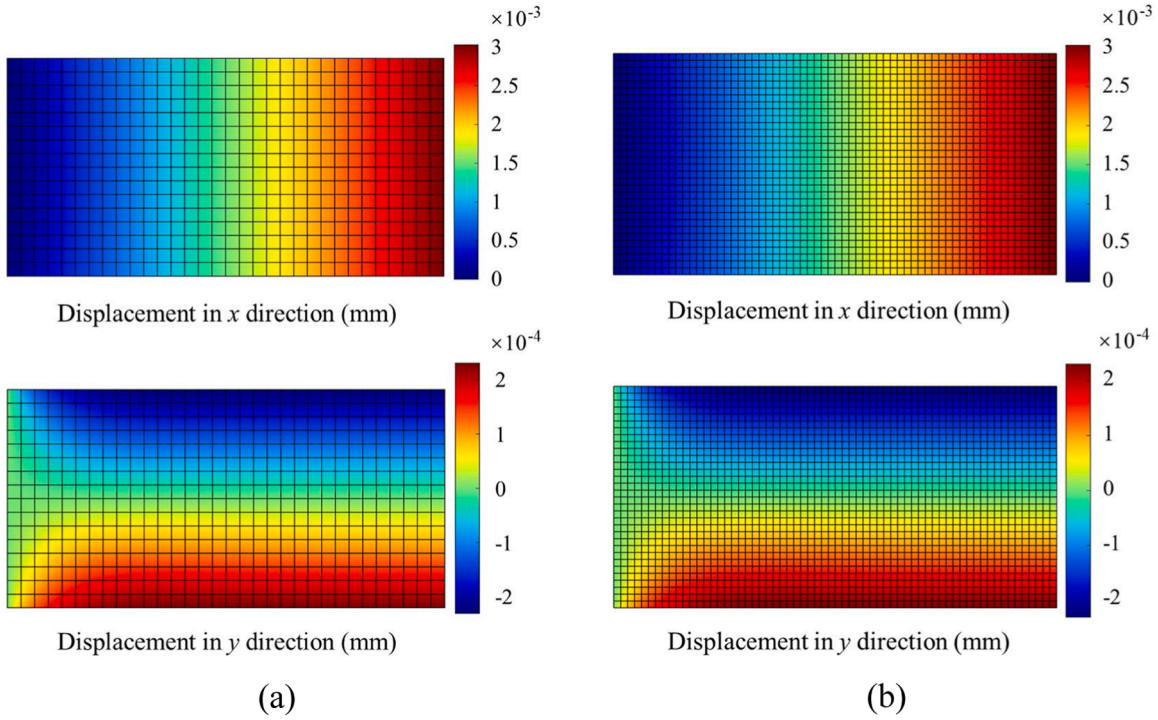


Fig. A3. Displacement results for the 2D plate: (a) IGA, (b) FEA.

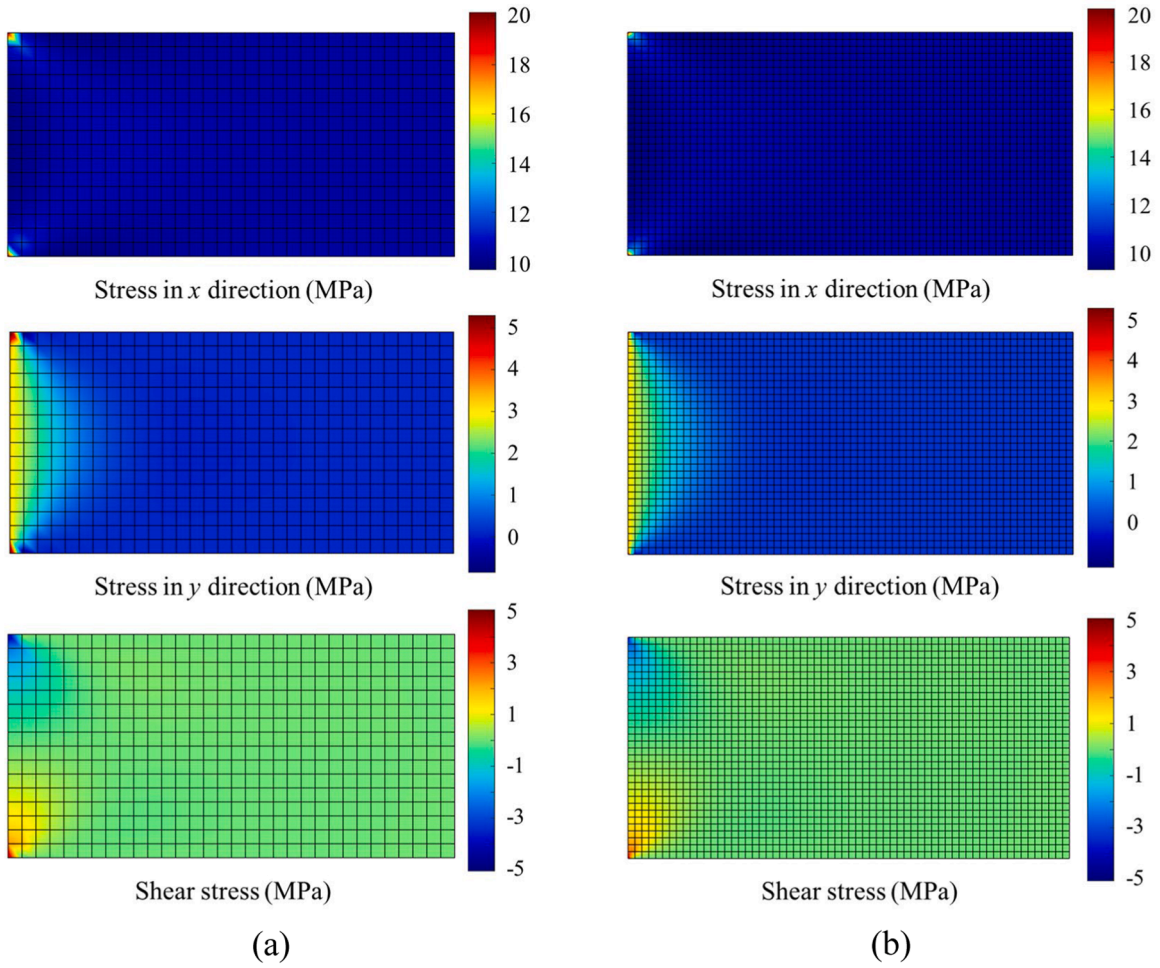


Fig. A4. Stress results for the 2D plate: (a) IGA, (b) FEA.

Appendix B. Supplementary to isogeometric structural mechanical analysis

For 2D structural problems, the $\boldsymbol{B}$ matrix is expressed as follows:

$$\boldsymbol{B} = \begin{bmatrix} \frac{\partial N_1}{\partial x} & 0 & \cdots & \frac{\partial N_{nc}}{\partial x} & 0 \\ 0 & \frac{\partial N_1}{\partial y} & \cdots & 0 & \frac{\partial N_{nc}}{\partial y} \\ \frac{\partial N_1}{\partial x} & \frac{\partial N_1}{\partial y} & \cdots & \frac{\partial N_{nc}}{\partial x} & \frac{\partial N_{nc}}{\partial y} \end{bmatrix} \tag{B1}$$

and

$$\begin{bmatrix} \frac{\partial N_i}{\partial x} & \frac{\partial N_i}{\partial y} \end{bmatrix} = \begin{bmatrix} \frac{\partial N_i}{\partial u} & \frac{\partial N_i}{\partial v} \end{bmatrix} \boldsymbol{J}_1^{-1} \tag{B2}$$

where N_i is the basis function of the NURBS element and nc denotes the number of control points for each element.

The Jacobi matrix $\boldsymbol{J}_1$ is calculated by the following equation:

$$\boldsymbol{J}_1 = \begin{bmatrix} \frac{\partial x_i}{\partial u} & \frac{\partial y_i}{\partial u} \\ \frac{\partial x_i}{\partial v} & \frac{\partial y_i}{\partial v} \end{bmatrix} \tag{B3}$$

In addition, the mapping from the Gaussian quadrature domain to the NURBS parameter domain is:

$$\begin{cases} u = \dfrac{u_{i+1} - u_i}{2}(\overline{u} - 1) + u_i \\ v = \dfrac{v_{i+1} - v_i}{2}(\overline{v} - 1) + v_i \end{cases} \tag{B4}$$

The corresponding Jacobi matrix $\boldsymbol{J}_2$ is:

$$\boldsymbol{J}_2 = \begin{bmatrix} \dfrac{\partial u}{\partial \overline{u}} & \dfrac{\partial v}{\partial \overline{u}} \\ \dfrac{\partial u}{\partial \overline{v}} & \dfrac{\partial v}{\partial \overline{v}} \end{bmatrix} = \begin{bmatrix} \dfrac{u_{i+1} - u_i}{2} & 0 \\ 0 & \dfrac{v_{i+1} - v_i}{2} \end{bmatrix} \tag{B5}$$

Appendix C. Sensitivity analysis of the objective function

In this study, the objective function is the compliance minimization of the entire structure, and its first-order sensitivity with respect to the design variables is given by:

$$\frac{\partial c(\boldsymbol{\rho})}{\partial \rho_e^{ij}} = \frac{\partial c(\boldsymbol{\rho})}{\partial \rho_e} \frac{\partial \rho_e}{\partial \widehat{\rho}_e^{ij}} \frac{\partial \widehat{\rho}_e^{ij}}{\partial \overline{\rho}_e^{ij}} \frac{\partial \overline{\rho}_e^{ij}}{\partial \rho_e^{ij}} \tag{C1}$$

where $\frac{\partial c(\boldsymbol{\rho})}{\partial \rho_e}$ and $\frac{\partial \rho_e}{\partial \widehat{\rho}_e^{ij}}$ are calculated from Eqs. (31) and (25), respectively.

$$\frac{\partial c(\boldsymbol{\rho})}{\partial \rho_e} = -pp(\rho_e)^{pp-1}(E_0 - E_{\min})(\boldsymbol{u}_e)_1^{\mathrm{T}} \boldsymbol{k}_0 (\boldsymbol{u}_e)_1 \tag{C2}$$

$$\frac{\partial \rho_e}{\partial \widehat{\rho}_e^{ij}} = \sum_{i=1}^{n} \sum_{j=1}^{m} N_{i,p}^{j,q}(\xi_e, \eta_e) \tag{C3}$$

Furthermore, $\frac{\partial \widehat{\rho}_e^{ij}}{\partial \overline{\rho}_e^{ij}}$ is derived from the Heaviside function:

$$\frac{\partial \widehat{\rho}_e^{ij}}{\partial \overline{\rho}_e^{ij}} = \frac{\beta\left(\operatorname{sech}\left(\beta(\overline{\rho}_e^{ij} - \alpha)\right)\right)^2}{\tanh(\beta\alpha) + \tanh(\beta(1-\alpha))} \tag{C4}$$

Finally, $\frac{\partial \overline{\rho}_e^{ij}}{\partial \rho_e^{ij}}$ is generated from the density filter Eq. (27) as follows:

$$\frac{\partial \overline{\rho}_e^{ij}}{\partial \rho_e^{ij}} = \frac{w_{ij,l}}{\sum_{la \in N_{ij}} w_{ij,la}} \tag{C5}$$

Appendix D. Sensitivity analysis of the volume constraint function

The volume constraint function depends only on the relative densities of the filtering function and the Heaviside function mapping. Therefore, the first-order sensitivity of the volume constraint function to the design variables is given by:

$$\frac{\partial V(\boldsymbol{\rho})}{\partial \rho_e^{ij}} = \frac{\partial V(\boldsymbol{\rho})}{\partial \rho_e} \frac{\partial \rho_e}{\partial \widehat{\rho}_e^{ij}} \frac{\partial \widehat{\rho}_e^{ij}}{\partial \overline{\rho}_e^{ij}} \frac{\partial \overline{\rho}_e^{ij}}{\partial \rho_e^{ij}} \tag{D1}$$

where $\frac{\partial V(\boldsymbol{\rho})}{\partial \rho_e}$ can be obtained according to Eq. (24).

$$\frac{\partial V(\boldsymbol{\rho})}{\partial \rho_e} = v_e \tag{D2}$$

Further, the sensitivity of the volume constraint function can be derived according to Eqs. (C3), (C4) and (C5) as follows:

$$\frac{\partial V(\boldsymbol{\rho})}{\partial \rho_e^{ij}} = v_e \sum_{i=1}^{n} \sum_{j=1}^{m} N_{i,p}^{j,q}(\xi_e, \eta_e) \frac{\beta\left(\operatorname{sech}\left(\beta(\overline{\rho}_e^{ij} - \alpha)\right)\right)^2}{\tanh(\beta\alpha) + \tanh(\beta(1-\alpha))} \frac{w_{ij,l}}{\sum_{la \in N_{ij}} w_{ij,la}} \tag{D3}$$

Data availability

Data will be made available on request.

References

[1] Y. Wang, X. Li, K. Long, P. Wei, Open-source codes of topology optimization: a summary for beginners to start their research, Comput. Model. Eng. Sci. 137 (1) (2023) 1–34.
[2] J.D. Deaton, R.V. Grandhi, A survey of structural and multidisciplinary continuum topology optimization: post 2000, Struct. Multidiscip. Optim. 49 (1) (2013) 1–38.
[3] M.P. Bendsøe, N. Kikuchi, Generating optimal topologies in structural design using a homogenization method, Comput. Methods Appl. Mech. Eng. 71 (2) (1988) 197–224.
[4] O. Sigmund, A 99 line topology optimization code written in Matlab, Struct. Multidiscip. Optim. 21 (2) (2001) 120–127.
[5] X. Huang, Y.M. Xie, M.C. Burry, Advantages of bi-directional evolutionary structural optimization (BESO) over evolutionary structural optimization (ESO), Adv. Struct. Eng. 10 (6) (2007) 727–737.
[6] P. Wei, Z. Li, X. Li, M.Y. Wang, An 88-line MATLAB code for the parameterized level set method based topology optimization using radial basis functions, Struct. Multidiscip. Optim. 58 (2) (2018) 831–849.
[7] W. Zhang, J. Chen, X. Zhu, J. Zhou, D. Xue, X. Lei, X. Guo, Explicit three dimensional topology optimization via Moving Morphable Void (MMV) approach, Comput. Methods Appl. Mech. Eng. 322 (2017) 590–614.
[8] X. Guo, W. Zhang, W. Zhong, Doing topology optimization explicitly and geometrically—a new moving morphable components based framework, J. Appl. Mech. 81 (8) (2014) 081009.
[9] E. Andreassen, A. Clausen, M. Schevenels, B.S. Lazarov, O. Sigmund, Efficient topology optimization in MATLAB using 88 lines of code, Struct. Multidiscip. Optim. 43 (1) (2010) 1–16.
[10] T.T. Banh, S. Shin, J. Kang, D. Lee, Frequency-constrained topology optimization in incompressible multi-material systems under design-dependent loads, Thin-Walled Struct. 196 (2024) 111467.
[11] H. Liu, Z. Zhang, B. Li, M. Xie, J. Hong, S. Zheng, Topology optimization of high frequency vibration problems using the EFEM-based approach, Thin-Walled Struct. 160 (2021) 107324.
[12] A. Verbart, M. Langelaar, F.v. Keulen, Damage approach: A new method for topology optimization with local stress constraints, Struct. Multidiscip. Optim. 53 (5) (2015) 1081–1098.
[13] A. Verbart, M. Langelaar, F.v. Keulen, A unified aggregation and relaxation approach for stress-constrained topology optimization, Struct. Multidiscip. Optim. 55 (2) (2016) 663–679.
[14] J.A. Norato, H.A. Smith, J.D. Deaton, R.M. Kolonay, A maximum-rectifier-function approach to stress-constrained topology optimization, Struct. Multidiscip. Optim. 65 (10) (2022) 286.
[15] M.-N. Nguyen, J. Kang, S. Shin, D. Lee, Dynamic-constrained multi-material topology optimization under heat flux and thermal–mechanical loading, Thin-Walled Struct. 193 (2023) 111218.
[16] J. Alexandersen, A detailed introduction to density-based topology optimisation of fluid flow problems with implementation in MATLAB, Struct. Multidiscip. Optim. 66 (1) (2023) 12.
[17] J. Hu, W. Li, J. Li, X. Chen, S. Yao, X. Huang, Topology optimization of porous structures by considering acoustic and mechanical characteristics, Eng. Struct. 295 (2023) 116843.
[18] Z. Liang, X. Wang, Y. Cui, W. Xu, Y. Zhang, Y. He, A new data-driven probabilistic fatigue life prediction framework informed by experiments and multiscale simulation, Int. J. Fatigue 174 (2023) 107731.
[19] E. Santecchia, A.M.S. Hamouda, F. Musharavati, E. Zalnezhad, M. Cabibbo, M. El Mehtedi, S. Spigarelli, A review on fatigue life prediction methods for metals, Adv. Mater. Sci. Eng. 2016 (2016) 1–26.
[20] J. Hou, J. Zhu, J. Wang, W. Zhang, Topology optimization of the multi-fasteners jointed structure considering fatigue constraints, Int. J. Simul. Multidiscip. Des. Optim. 9 (2018) A4.
[21] H. Xie, G. Yang, J. Sun, W. Sai, W. Zeng, Anti-fatigue optimization of the twisting force arm of landing gear based on Kriging approximate sequential optimization method, J. Chinese Inst. Eng. 47 (1) (2023) 1–11.
[22] Y. Chen, Q. Wang, C. Wang, P. Gong, Y. Shi, Y. Yu, Z. Liu, Topology optimization design and experimental research of a 3D-printed metal aerospace bracket considering fatigue performance, Appl. Sci. 11 (15) (2021) 6671.
[23] C. Boursier Niutta, A. Tridello, G. Barletta, N. Gallo, A. Baroni, F. Berto, D. S. Paolino, Defect-driven topology optimization for fatigue design of additive manufacturing structures: application on a real industrial aerospace component, Eng. Fail. Anal. 142 (2022) 106737.
[24] S. Demir, M. Kurt, T. Kotil, Fatigue damage–based topology optimization of helicopter tail rotor pitch arm, J. Aerosp. Eng. 35 (5) (2022) 04022073.
[25] C. Boursier Niutta, A. Tridello, D.S. Paolino, Fatigue design of additive manufacturing components through topology optimization: comparison of methodologies based on the defect distribution and on the stress gradient, Fatigue Fract. Eng. Mater. Struct. 46 (9) (2023) 3429–3445.
[26] X. Tian, G. Liu, W. Deng, Y. Xie, H. Wang, Fatigue constrained topology optimization for the jacket support structure of offshore wind turbine under the dynamic load, Appl. Ocean Res. 142 (2024) 103812.
[27] B. Desmorat, R. Desmorat, Topology optimization in damage governed low cycle fatigue, Comptes Rendus Mécanique 336 (5) (2008) 448–453.
[28] K. Sherif, W. Witteveen, K. Puchner, H. Irschik, Efficient topology optimization of large dynamic finite element systems using fatigue, AIAA J. 48 (7) (2010) 1339–1347.
[29] K.A. James, H. Waisman, Failure mitigation in optimal topology design using a coupled nonlinear continuum damage model, Comput. Methods Appl. Mech. Eng. 268 (2014) 614–631.
[30] M. Collet, M. Bruggi, P. Duysinx, Topology optimization for minimum weight with compliance and simplified nominal stress constraints for fatigue resistance, Struct. Multidiscip. Optim. 55 (3) (2016) 839–855.
[31] K. Nabaki, J. Shen, X. Huang, Evolutionary topology optimization of continuum structures considering fatigue failure, Mater. Des. 166 (2019) 107586.
[32] K. Nabaki, J. Shen, X. Huang, Effect of different fatigue constraints on optimal topology of structures with minimum weight, Eng. Struct. 288 (2023) 116149.
[33] S.H. Jeong, S.H. Park, D.-H. Choi, G.H. Yoon, Topology optimization considering static failure theories for ductile and brittle materials, Comput. Struct. 110-111 (2012) 116–132.
[34] S.H. Jeong, D.-H. Choi, G.H. Yoon, Fatigue and static failure considerations using a topology optimization method, Appl. Math. Modell. 39 (3-4) (2015) 1137–1162.
[35] J.W. Lee, G.H. Yoon, S.H. Jeong, Topology optimization considering fatigue life in the frequency domain, Comput. Math. Appl. 70 (8) (2015) 1852–1877.
[36] S.H. Jeong, J.W. Lee, G.H. Yoon, D.H. Choi, Topology optimization considering the fatigue constraint of variable amplitude load based on the equivalent static load approach, Appl. Math. Modell. 56 (2018) 626–647.
[37] Y. Chen, E. Monteiro, I. Koutiri, V. Favier, Stress-constrained topology optimization using the constrained natural element method, Struct. Multidiscip. Optim. 67 (4) (2024) 65.
[38] Y. Chen, E. Monteiro, I. Koutiri, V. Favier, Fatigue-constrained topology optimization using the constrained natural element method, Comput. Methods Appl. Mech. Eng. 422 (2024) 116821.
[39] X. Gao, R. Caivano, A. Tridello, G. Chiandussi, H. Ma, D. Paolino, F. Berto, Innovative formulation for topological fatigue optimisation based on material defects distribution and TopFat algorithm, Int. J. Fatigue 147 (2021) 106176.
[40] T. Zhao, Y. Zhang, Y. Ou, W. Ding, F. Cheng, Fail-safe topology optimization considering fatigue, Struct. Multidiscip. Optim. 66 (6) (2023) 132.
[41] L. Li, G. Zhang, K. Khandelwal, Topology optimization of energy absorbing structures with maximum damage constraint, Int. J. Numer. Methods Eng. 112 (7) (2017) 737–775.
[42] L. Li, G. Zhang, K. Khandelwal, Failure resistant topology optimization of structures using nonlocal elastoplastic-damage model, Struct. Multidiscip. Optim. 58 (4) (2018) 1589–1618.
[43] S. Suresh, S.B. Lindström, C.-J. Thore, A. Klarbring, Acceleration of continuous-time, high-cycle fatigue constrained problems in topology optimization, Eur. J. Mech. - A/Solids 96 (2022) 104723.
[44] E. Holmberg, B. Torstenfelt, A. Klarbring, Fatigue constrained topology optimization, Struct. Multidiscip. Optim. 50 (2) (2014) 207–219.
[45] K.A. James, H. Waisman, Topology optimization of structures under variable loading using a damage superposition approach, Int. J. Numer. Methods Eng. 101 (5) (2015) 375–406.
[46] J. Oest, E. Lund, Topology optimization with finite-life fatigue constraints, Struct. Multidiscip. Optim. 56 (5) (2017) 1045–1059.
[47] J. Oest, R. Sørensen, L.C.T. Overgaard, E. Lund, Structural optimization with fatigue and ultimate limit constraints of jacket structures for large offshore wind turbines, Struct. Multidiscip. Optim. 55 (3) (2016) 779–793.
[48] S. Zhang, C. Le, A.L. Gain, J.A. Norato, Fatigue-based topology optimization with non-proportional loads, Comput. Methods Appl. Mech. Eng. 345 (2019) 805–825.
[49] Z. Chen, K. Long, P. Wen, S. Nouman, Fatigue-resistance topology optimization of continuum structure by penalizing the cumulative fatigue damage, Adv. Eng. Softw. 150 (2020) 102924.
[50] Z. Chen, K. Long, C. Zhang, X. Yang, F. Lu, R. Wang, B. Zhu, X. Zhang, A fatigue-resistance topology optimization formulation for continua subject to general loads using rainflow counting, Struct. Multidiscip. Optim. 66 (9) (2023) 210.
[51] P. Tauzowski, B. Błachowski, J. Lógó, Optimal topologies considering fatigue with reliability constraint, Adv. Eng. Softw. 189 (2024) 103590.
[52] J. Gu, Z. Chen, K. Long, Y. Wang, Nonlinear fatigue damage constrained topology optimization, Comput. Methods Appl. Mech. Eng. 429 (2024) 117136.
[53] S.M. Hermansen, E. Lund, Multi-material and thickness optimization of laminated composite structures subject to high-cycle fatigue, Struct. Multidiscip. Optim. 66 (12) (2023) 259.
[54] F. Dirksen, M. Anselmann, T.I. Zohdi, R. Lammering, Incorporation of flexural hinge fatigue-life cycle criteria into the topological design of compliant small-scale devices, Precis. Eng. 37 (3) (2013) 531–541.
[55] X. Teng, C. Wang, X. Jiang, X. Chen, Structural topology optimization with local finite-life fatigue constraints, Mathematics 11 (5) (2023) 1220.
[56] T.J.R. Hughes, J.A. Cottrell, Y. Bazilevs, Isogeometric analysis: CAD, finite elements, NURBS, exact geometry and mesh refinement, Comput. Methods Appl. Mech. Eng. 194 (39-41) (2005) 4135–4195.
[57] V.N.V. Do, T.H. Ong, C.-H. Lee, Isogeometric analysis for nonlinear buckling of FGM plates under various types of thermal gradients, Thin-Walled Struct. 137 (2019) 448–462.
[58] Y.-D. Seo, H.-J. Kim, S.-K. Youn, Isogeometric topology optimization using trimmed spline surfaces, Comput. Methods Appl. Mech. Eng. 199 (49-52) (2010) 3270–3296.
[59] L. Dedè, M.J. Borden, T.J.R. Hughes, Isogeometric analysis for topology optimization with a phase field model, Arch. Comput. Method. Eng. 19 (3) (2012) 427–465.
[60] Y. Wang, D.J. Benson, Isogeometric analysis for parameterized LSM-based structural topology optimization, Comput. Mech. 57 (1) (2016) 19–35.
[61] Y. Wang, H. Xu, D. Pasini, Multiscale isogeometric topology optimization for lattice materials, Comput. Methods Appl. Mech. Eng. 316 (2017) 568–585.

[62] Y. Wang, M. Xiao, Z. Xia, P. Li, L. Gao, From computer-aided design (CAD) toward human-aided design (HAD): an isogeometric topology optimization approach, Engineering 22 (2023) 94–105.
[63] J. Gao, L. Gao, Z. Luo, P. Li, Isogeometric topology optimization for continuum structures using density distribution function, Int. J. Numer. Methods Eng. 119 (10) (2019) 991–1017.
[64] J. Gao, H. Xue, L. Gao, Z. Luo, Topology optimization for auxetic metamaterials based on isogeometric analysis, Comput. Methods Appl. Mech. Eng. 352 (2019) 211–236.
[65] W. Hou, Y. Gai, X. Zhu, X. Wang, C. Zhao, L. Xu, K. Jiang, P. Hu, Explicit isogeometric topology optimization using moving morphable components, Comput. Methods Appl. Mech. Eng. 326 (2017) 694–712.
[66] W. Qiu, Q. Wang, L. Gao, Z. Xia, Evolutionary topology optimization for continuum structures using isogeometric analysis, Struct. Multidiscip. Optim. 65 (4) (2022) 121.
[67] B. Li, S. Ding, S. Guo, W. Su, A. Cheng, J. Hong, A novel isogeometric topology optimization framework for planar compliant mechanisms, Appl. Math. Modell. 92 (2021) 931–950.
[68] D. Villalba, J. París, I. Couceiro, F. Navarrina, Isogeometric topology optimization of structures using the overweight approach, Struct. Multidiscip. Optim. 67 (5) (2024) 84.
[69] P. Kang, S.-K. Youn, Isogeometric topology optimization of shell structures using trimmed NURBS surfaces, Finite Element. Anal. Des. 120 (2016) 18–40.
[70] X. Zhang, M. Xiao, L. Gao, J. Gao, A T-splines-oriented isogeometric topology optimization for plate and shell structures with arbitrary geometries using Bézier extraction, Comput. Methods Appl. Mech. Eng. 425 (2024) 116929.
[71] W. Qiu, Q. Wang, L. Gao, Z. Xia, Stress-based evolutionary topology optimization via XIGA with explicit geometric boundaries, Int. J. Mech. Sci. 256 (2023) 108512.
[72] Q.X. Lieu, J. Lee, A multi-resolution approach for multi-material topology optimization based on isogeometric analysis, Comput. Methods Appl. Mech. Eng. 323 (2017) 272–302.
[73] A.H. Taheri, K. Suresh, An isogeometric approach to topology optimization of multi-material and functionally graded structures, Int. J. Numer. Methods Eng. 109 (5) (2017) 668–696.
[74] H.A. Jahangiry, M. Gholhaki, H. Naderpour, S.M. Tavakkoli, Isogeometric level set topology optimization for elastoplastic plane stress problems, Int. J. Mech. Mater. Des. 17 (4) (2021) 947–967.
[75] H.A. Jahangiry, M. Gholhaki, H. Naderpour, S.M. Tavakkoli, Isogeometric level set-based topology optimization for geometrically nonlinear plane stress problems, Comput.-Aid. Des. 151 (2022) 103358.
[76] X. Zhai, Alternating optimization method for isogeometric topology optimization with stress constraints, J. Comput. Math. 42 (1) (2024) 134–155.
[77] H. Liu, D. Yang, P. Hao, X. Zhu, Isogeometric analysis based topology optimization design with global stress constraint, Comput. Methods Appl. Mech. Eng. 342 (2018) 625–652.
[78] D. Villalba, M. Gonçalves, J. Dias-de-Oliveira, A. Andrade-Campos, R. Valente, IGA-based topology optimization in the design of stress-constrained compliant mechanisms, Struct. Multidiscip. Optim. 66 (12) (2023) 244.
[79] C. Zhuang, Z. Xiong, H. Ding, Stress-related topology optimization with multilevel smoothed isogeometric densities and Bézier elements, Comput. Methods Appl. Mech. Eng. 409 (2023) 115974.
[80] K. Svanberg, The method of moving asymptotes—a new method for structural optimization, Int. J. Numer. Methods Eng. 24 (2) (1987) 359–373.
[81] K.-T. Zuo, L.-P. Chen, Y.-Q. Zhang, J. Yang, Study of key algorithms in topology optimization, Int. J. Adv. Manuf. Technol. 32 (7-8) (2006) 787–796.
[82] V.P. Nguyen, C. Anitescu, S.P. Bordas, T. Rabczuk, Isogeometric analysis: an overview and computer implementation aspects, Math. Comput. Simul. 117 (2015) 89–116.
[83] J. Xu, L. Gao, M. Xiao, J. Gao, H. Li, Isogeometric topology optimization for rational design of ultra-lightweight architected materials, Int. J. Mech. Sci. 166 (2020) 105103.
[84] P. Fischer, M. Klassen, J. Mergheim, P. Steinmann, R. Müller, Isogeometric analysis of 2D gradient elasticity, Comput. Mech. 47 (3) (2010) 325–334.
[85] D. Rypl, B. Patzák, From the finite element analysis to the isogeometric analysis in an object oriented computing environment, Adv. Eng. Softw. 44 (1) (2012) 116–125.
[86] J.A. Cottrell, T.J. Hughes, Y. Bazilevs, Isogeometric Analysis: Toward Integration of CAD and FEA, John Wiley & Sons, 2009.
[87] R. Pawliczek, D. Rozumek, The effect of mean load for S355J0 steel with increased strength, Metals. (Basel) 10 (2) (2020) 209.
[88] F. Wang, B.S. Lazarov, O. Sigmund, On projection methods, convergence and robust formulations in topology optimization, Struct. Multidiscip. Optim. 43 (6) (2011) 767–784.
[89] B. Bourdin, Filters in topology optimization, Int. J. Numer. Methods Eng. 50 (9) (2001) 2143–2158.
[90] T.E. Bruns, D.A. Tortorelli, Topology optimization of non-linear elastic structures and compliant mechanisms, Comput. Methods Appl. Mech. Eng. 190 (26-27) (2001) 3443–3459.
[91] Y. Han, B. Xu, Z. Duan, X. Huang, Stress-based bi-directional evolutionary structural topology optimization considering nonlinear continuum damage, Comput. Methods Appl. Mech. Eng. 396 (2022) 115086.
[92] C. Le, J. Norato, T. Bruns, C. Ha, D. Tortorelli, Stress-based topology optimization for continua, Struct. Multidiscip. Optim. 41 (4) (2009) 605–620.
[93] M. Kočvara, M. Stingl, Solving stress constrained problems in topology and material optimization, Struct. Multidiscip. Optim. 46 (1) (2012) 1–15.
[94] E. Holmberg, B. Torstenfelt, A. Klarbring, Stress constrained topology optimization, Struct. Multidiscip. Optim. 48 (1) (2013) 33–47.
[95] X. Du, G. Zhao, W. Wang, M. Guo, R. Zhang, J. Yang, NLIGA: A MATLAB framework for nonlinear isogeometric analysis, Comput. Aided. Geom. Des. 80 (2020) 101869.